ORIGINAL ARTICLE

Thm2 interacts with paralog, *Thm1*, and sensitizes to Hedgehog signaling in postnatal skeletogenesis

Bailey A. Allard[1] · Wei Wang[1] · Tana S. Pottorf[1] · Hammad Mumtaz[3] · Brittany M. Jack[1] · Henry H. Wang[1] · Luciane M. Silva[1] · Damon T. Jacobs[1] · Jinxi Wang[2] · Erin E. Bumann[3] · Pamela V. Tran[1]

Abstract
Mutations in the intraflagellar transport-A (IFT-A) gene, *THM1*, have been identified in skeletal ciliopathies. Here, we report a genetic interaction between *Thm1*, and its paralog, *Thm2,* in postnatal skeletogenesis. THM2 localizes to primary cilia, but *Thm2* deficiency does not affect ciliogenesis and *Thm2*-null mice survive into adulthood. However, by postnatal day 14, *Thm2*$^{-/-}$; *Thm1*$^{aln/+}$ mice exhibit small stature and small mandible. Radiography and microcomputed tomography reveal *Thm2*$^{-/-}$; *Thm1*$^{aln/+}$ tibia are less opaque and have reduced cortical and trabecular bone mineral density. In the mutant tibial growth plate, the proliferation zone is expanded and the hypertrophic zone is diminished, indicating impaired chondrocyte differentiation. Additionally, mutant growth plate chondrocytes show increased Hedgehog signaling. Yet deletion of one allele of *Gli2*, a major transcriptional activator of the Hedgehog pathway, exacerbated the *Thm2*$^{-/-}$; *Thm1*$^{aln/+}$ small phenotype, and further revealed that *Thm2*$^{-/-}$; *Gli2*$^{+/-}$ mice have small stature. In *Thm2*$^{-/-}$; *Thm1*$^{aln/+}$ primary osteoblasts, a Hedgehog signaling defect was not detected, but bone nodule formation was markedly impaired. This indicates a signaling pathway is altered, and we propose that this pathway may potentially interact with *Gli2*. Together, our data reveal that loss of *Thm2* with one allele of *Thm1, Gli2,* or both, present new IFT mouse models of osteochondrodysplasia. Our data also suggest *Thm2* as a modifier of Hedgehog signaling in postnatal skeletal development.

Keywords Ttc21a · Ttc21b · Knock-out · CRISPR · Cell-specific

Introduction

Skeletal dysplasias affect 1:5000 births and range in severity from perinatal lethality to craniofacial dysmorphogenesis and short stature. These disorders are often heritable, and identifying the causative mutations has been instrumental in improving diagnosis, understanding the mode of inheritance, and identifying therapeutic targets.

✉ Pamela V. Tran
  ptran@kumc.edu

[1] Department of Anatomy and Cell Biology, Jared Grantham Kidney Institute, University of Kansas Medical Center, 3901 Rainbow Blvd., MS #3038, Kansas City, KS 66160, USA

[2] Department of Orthopedic Surgery, Medical Center, University of Kansas, Kansas City, KS 66160, USA

[3] Department of Oral and Craniofacial Sciences, School of Dentistry, University of Missouri-Kansas City, Kansas City, MO, USA

Conversely, genetic disorders that cause skeletal dysplasias provide valuable insight into underlying molecular and cellular mechanisms. One such class of genetic disorders are ciliopathies, which result from mutation and dysfunction of primary cilia. The primary cilium is a solitary, sensory organelle that protrudes from the surface of most mammalian cells, including bone and cartilage cells [1, 2]. As such, ciliopathies affect multiple organ systems, and a proportion of ciliopathies manifest osteochondrodysplasias [3, 4]. These skeletal ciliopathies include Short-Rib Polydactyly Syndromes (I–IV), Jeune Syndrome, Oro-facial-digital syndrome type 1, Ellis van Creveld syndrome, and cranioectodermal dysplasia (also known as Sensenbrenner Syndrome), which manifest to varying degrees, shortened long bones, narrow rib cage, polydactyly and craniofacial defects. Fibrocystic diseases of the kidney, liver and pancreas can also arise. These ciliopathies reveal that primary cilia are potent modifiers of skeletal growth.

Primary cilia detect and transduce extracellular mechanical and chemical cues into signaling cascades to ultimately

affect cellular behavior [5, 6]. These antenna-like organelles are dynamic structures, formed and maintained by intraflagellar transport (IFT), which is the bi-directional transport of cargo (structural and signaling proteins) by multiprotein complexes along a microtubular axoneme. IFT-B proteins, together with the kinesin motor, transport cargo from the base to the tip of the cilium in anterograde IFT, while IFT-A proteins and the dynein motor are required to return proteins from the ciliary tip to the base in retrograde IFT. IFT-A proteins also mediate ciliary entry of membrane-associated and signaling proteins [7–10]. Primary cilia transduce the Hedgehog (Hh) signal [11]. The presence of Hh ligand induces ciliary enrichment of the Smoothened signal transducer and culminates in activation of the *Gli* transcription factors, of which GLI2 is the primary transcriptional activator [12, 13]. The differing roles of IFT-B versus -A can result in contrasting ciliary and Hh signaling phenotypes in *Ift* mutant mouse embryos. Loss of IFT-B or kinesin, generally results in loss of cilia and Hh activity, and mid-gestational lethality [14–16], while deletion of IFT-A causes shortened primary cilia with protein accumulation in a bulbous distal tip. Further, two IFT-A mouse embryonic mutants show overactivation of the Hh pathway, and perinatal lethality [17, 18]. Yet in contrast to these earlier reports, deletion of kinesin subunit, *Kif3a*, in neural crest cells increased GLI activity in the frontonasal prominence of the developing face [19], while deletion of IFT-A gene, *Thm1*, in glial cells decreased Hh signaling in the developing cerebellum [20]. Thus, whether an IFT protein positively or negatively regulates Hh or GLI activity is cell-specific and/or context-dependent.

In patients with skeletal ciliopathies, mutations have been identified in all of the six characterized IFT-A components (*IFT43* [21, 22], *IFT121* [22], *IFT122* [23, 24], *WDR19/IFT144* [25]*, IFT140* [26]*,* and *THM1* [27]) and in 4 of the 14 IFT-B components (*IFT80* [28], *IFT52* [29, 30], *IFT172* [4] and *IFT56* [31]. In accordance with the human genetics studies, many of the reported IFT-A mouse mutants have exhibited polydactyly and abnormal development of the thoracic ribs during embryogenesis [32–34]. Additionally, *Ift80*-hypomorphic mice that survive past birth, and mice with conditional deletion of IFT-B gene, *Ift88,* in the limb bud and craniofacial mesenchyme, exhibit polydactyly, shortened long bones, and disorganization of the growth plate [35, 36]. Thus, both IFT-B and -A are essential for mammalian skeletal growth, although the human genetics studies may suggest that IFT-A mutations are more compatible with life.

Previously, we identified *THM1* (TPR-containing Hh modulator 1; also known as *TTC21B*) as an IFT-A component and regulator of Hh signaling [17]. A germ-line mutation resulting in THM1 loss in mouse causes shortened long bones, split and fused ribs, and polydactyly. *THM1*

mutations have also been identified in patients with Jeune Syndrome (JATD) [18], which is characterized by shortened long bones, craniofacial defects, and a narrow rib cage that often inhibits lung development and causes 60–80% mortality among infants and children [37]. We also identified a paralog of *THM1*, which we call *THM2* (also known as *TTC21A*) [17]. THM1 and THM2 are orthologues of the IFT-A protein, IFT139, in *Chlamydomonas reinhardtii*, and have similar levels of homology to *IFT139/FLA16. Thm1* and *Thm2* have similar predicted protein structures with multiple TPR domains and similar RNA expression patterns during mouse development. A recent report revealed that *THM2* is required for male fertility [38]. However, a role for *Thm2* in early postnatal development has not been elucidated. Here by generating in vitro and in vivo models of *Thm2* deficiency and implementing genetic crosses, we reveal a role for THM2 in postnatal skeletogenesis.

Methods

Generation of THM2 knockdown cell line

Lentiviral transfection was used to generate a human embryonic kidney (293T) *THM2* knockdown cell line. Briefly, viral particles were created by transfecting three plasmids, 4.2 µg vector (*Thm2* shRNA sequence GACTTTGATTAATTA CTAT), 7.4 µg delta 8.2 and 0.4 µg VSVG into 293T packaging cells using the Fugene transfection reagent (Promega, E2691) into 293T cells. After 48 h, media was collected and filtered to obtain viral particles. This media containing virus was placed onto 293T target cells for 6 h and then replaced by fresh media. Infected cells were selected using 1 µg/ml puromycin. After reaching confluence, cells were trysinized, resuspended, then seeded sparsely onto 25 cm dishes to allow individual clones to grow. Clones were selected using cloning disks immersed in Trypsin. Clones were then expanded.

Western blot

293T cells and mouse tissues were collected. Protein was extracted by resuspending cells or homogenizing tissue in passive lysis buffer (Promega, E1941) containing protease inhibitors (Thermo Scientific, 88669), and rocking samples for 15 min at room temperature. Lysed cells and tissues were pelleted and supernatants were collected. Protein concentration of lysates was determined using the Pierce BCA Protein Assay Kit (ThermoFisher, 23227). Lysates with loading dye were boiled for 5 min, cooled on ice, and loaded onto a 4–20% SDS-gel (BioRad, 456-8094). Gels were run for approximately 3.5 h at 90 V to adequately separate protein. Membranes were incubated with THM2 antibody using

Western blot as described [17]. THM2 antibody was targeted to *N′* Cys-RRQNYETAINLYHQVLEK, 963-980aa, in exon 22. (Proteintech S4132-2, 1:5000).

Immunofluorescence

Retinal pigment epithelial (RPE) cells, 293T cells, and primary chondrocytes and osteoblasts were seeded onto poly-L-lysine coated coverslips in 24-well plates. Confluent RPE and 293 T cells were serum-starved overnight to increase cilia lengths. All post-confluent cells were fixed in 4% PFA in PBS containing 0.1% Triton x-100 for 10 min at room temperature, then blocked in 1% Bovine Serum Albumin (Sigma, A9647) for 1 h. Primary antibodies against Arl13b (Proteintech, 17711-1-AP, 1:300), acetylated α-tubulin (Sigma T6557, 1:4000), THM2 (Custom-made Antibody, Proteintech S4132-2, 1:50), IFT81 (Proteintech, 11744-1-AP, 1:200), SMO (Santa Cruz, sc-166685, 1:50) were incubated with cells in 1% BSA overnight at 4°C. Cells were washed three times in PBS, then incubated with secondary antibody conjugated to Alexa Fluor 594 or Alexa Fluor 488 [Life Technologies, A-11005 (anti-mouse) and A-11008 (anti-rabbit), 1:500] for 1 h at room temperature. Cells were washed three times in PBS. Coverslips were inverted and mounted onto slides using DAPI Fluoromount-G (Electron Microscopy Services, 17984-24). RPE cells were imaged using a Nikon Eclipse TiE attached to an A1R-SHR confocal with an A1-DU4 detector and LU4 laser launch. All other cells were imaged using a Nikon 80i or Nikon TiS attached to a Nikon DS-Fi1 or QICAM FAST1934 camera, respectively.

Generation of Thm2 knockout mouse

Thm2 knockout-first C57BL/6J embryonic stem cells were obtained from the NIH Knockout Mouse Project (KOMP) Repository (www.komp.org). Embryonic stem cells were confirmed to contain the correct *Thm2* knockout construct showing evidence of homologous recombination and correct karyotype. Subsequently, cells were injected into C57BL/6J-*Tyr^{c-2J}* (albino) blastocysts and implanted into female mice by Dr. Melissa Larson at the University of Kansas Medical Center Transgenic and Gene Targeting Facility. Resulting male chimeras were mated to multiple females. Genomic DNA from tails of resulting pups with black coat color was genotyped by polymerase chain reaction (PCR) and PCR amplicons were sequenced to confirm the presence of the construct in the DNA. The KOMP allele contains a LacZ neo construct flanked by flippase recombinase (FLP) recombinase target (FRT) sites. Mice containing the KOMP construct were mated to a mouse carrying a FLP recombinase (Jackson Laboratories, 009086) to excise the LacZ-Neo cassette. Resulting mice were then mated to mice expressing

cytomegalovirus (CMV) Cre recombinase (Jackson Laboratories, 006064) to excise exon 6, which created a premature stop codon and a *Thm2* null allele. All animal procedures were conducted in accordance with KUMC-IACUC and AAALAC rules and regulations.

Genotyping of Thm2 knockout mouse

Genotyping primers were designed flanking the loxP sites surrounding exon 6. Primers *Thm2*-KO-F—5′ CAG ATA TCT CCC CAC TTG TTA ACG 3′ and *Thm2*-KO-R—5′ GTG TCA GAT ACC CTG GAA CCA GAG 3′ amplify a WT band of 1086 bp and a knockout band of approximately 400 bp. Since at times, this PCR reaction favors amplification of the smaller knockout band, making the WT band difficult to see, additional PCR primers, *Thm2*-WT-F-5′AAC TTC CTG CCC GCT TTA GT 3′ and *Thm2*-WT-R-5′ GTG TCA GAT ACC CTG GAA CCA GAG 3′ are used to amplify only a WT band of 461 bp.

Generation of Thm2$^{−/−}$;Thm1$^{aln/+}$ mice

Thm2$^{−/−}$;Thm1$^{aln/+}$ mice were generated by crossing *Thm2$^{+/-}$* mice on a C57BL/6 background with *Thm1$^{aln/+}$* mice on an FVB background. *Thm2$^{+/-}$;Thm1$^{aln/+}$* mice were then backcrossed five generations onto a C57BL6/J background.

Weight and length measurements

Total mouse body weight was measured using a standard laboratory weighing scale. Crown-to-rump measurements, from the tip of the nose to the end of the rump, were obtained using a standard ruler.

Skeletal preparations

Alizarin red and alcian blue staining of skeletons was performed as described [32]. Briefly, P14 mice were eviscerated and fixed in 95% ethanol for 1–2 days, then stained with alcian blue (Acros Organics 33864-99-2) for 14 days. Subsequently, skeletons were fixed in 95% ethanol for 1–2 days and cleared with potassium hydroxide for 2–5 days, or until the tissue was cleared. Skeletons were stained with 1% alizarin red (Acros Organics 130-22-3) in potassium hydroxide for 1–2 days or until staining was complete. Skeletons were then cleared in glycerol for imaging and long-term storage. Skeletal preparations were imaged using a dissecting scope (Leica M165C) and bone lengths were quantified using Image J software.

Microcomputed tomography and Faxitron

Whole mice and tibias were radiographed at 1X and 3X magnifications, respectively, using a LX-60 DC12 Cabinet X-ray System (Faxitron) at 26kVP for 10 s. Images were analyzed using ImageJ to calculate the length of each mineralized caudal vertebrae.

Ethanol-fixed tibia from control and triple allele mutant mice were scanned in a Skyscan 1174 micro-computed tomography system (Bruker) at a resolution of 14 μm^3 with a voltage of 50kVp using a 0.5 mm aluminum filter. Tibias were wrapped in gauze soaked with 70% ethanol and placed in a low-density polyethylene tube for scanning. Camera pixel binning was not applied and the integration time was set to 3000 ms. The scan orbit was 180°/360° with a rotation step of 0.3°. Reconstruction was carried out with a modified Feldkamp algorithm using the SkyScanTM NRecon software accelerated by GPU3. Gaussian smoothing, ring artifact reduction, and beam hardening correction were applied. Reconstructed images were analyzed by CTAn software. Irregular, anatomic regions of interest (ROIs) were selected for both trabecular and cortical bone analysis. For trabecular bone analysis, slices from the proximal tibia starting at the distal end of the growth plate to the end of the trabeculae were analyzed for bone mineral density (BMD), bone volume fraction (BV/TV), bone surface per BV (BS/BV), trabecular thickness (Tb. Th), separation (Tb.Sp), and number (Tb.N). For cortical bone analysis, two sets of ROIs were analyzed for BMD, total cross-sectional bone area (Tt.Ar), cortical bone area (Ct.Ar), fraction (Ct.Ar/Tt.Ar), perimeter (Ct.Pm), and thickness (Ct.Th). The first was from mid-diaphysis and the second started at the end of the trabeculae at the proximal end of the tibia. To control for length differences, the same percentage of slices were analyzed in mutants as relative length for both trabecular and cortical analysis. The minimum and maximum thresholds were set to 45 and 95 for trabecular bone analysis and 55 and 255 for cortical bone analysis.

Dissection, embedding and sectioning of tibias and soft organs

Tibias were dissected and placed in Cal-Ex, a decalcifying and fixing solution (Fisher C5511-1D), for 3 days. Kidney, heart and lung were dissected and weighed. Kidneys were fixed in Bouin's fixative (Polysciences, Inc. 16045) overnight. Following fixation, tibias and kidneys were placed into 70% ethanol. Tissues were processed and dehydrated through an ethanol series and embedded in paraffin wax. Paraffin blocks were sectioned at 10 μm and 7 μm for tibias and soft organs, respectively.

Hematoxylin and eosin and safarnin O and fast green staining

Tibia and kidney sections were de-paraffinized and rehydrated through an ethanol series. Sections were stained with Hematoxylin (Sigma HHS32) and Eosin (Sigma HT110216) or with Weigert's Hematoxylin, 0.2% Fast Green, and Safranin O. Sections were dehydrated through an ethanol series and mounted with Permanent Mounting Media (Fisher, SP15-500). Sections were imaged using a light microscope (Nikon 80i) attached to a Nikon DS-Fi1 camera.

Antigen retrieval

Prior to immunostaining, tissue sections were deparaffinized, rehydrated, and subjected to antigen retrieval. Tissue sections were steamed for 25 min in Sodium Citrate Buffer (10 mM Sodium Citrate, 0.05% Tween 20, pH 6.0). Sections were cooled and rinsed in distilled water ten times.

LacZ staining

Gli1-LacZ reporter mice (Jackson Laboratories, stock 008211) were crossed into the *Thm2; Thm1* colonies. Tibias were dissected, fixed in acetone for 48 h at 4°C as described [39]. Fixed tissues were immersed in wash buffer (100 mM sodium phosphate buffer (pH 7.3), 2 mM magnesium chloride, 0.02% Nonidet P-40, and 0.01% sodium deoxycholate) for 15 min, three times. Tibia were stained with X-gal solution (Teknova X1220; 1 mg/ml X-gal in *N,N*-dimethylformamide) in wash buffer containing 5 mM potassium ferrocyanide (Sigma P-9387) and 5 mM potassium ferricyanide (Sigma P-8131) protected from light overnight or until desired color intensity was obtained. Stained tibia were fixed and demineralized in CalEx, processed, embedded in paraffin, and sectioned as described above. Sections were rehydrated through an ethanol series, counterstained with nuclear fast red, and mounted. Stained sections were imaged using a Nikon 80i attached to a Nikon DS-Fi1 camera. Using ImageJ, colored images were converted to monochrome images using RGB stack, thresholds were obtained, and growth plates were demarcated for measurements of area, mean and integrated density to quantify LacZ staining of litter-matched sections of control and triple allele mutant growth plates.

Generation of primary chondrocytes and osteoblasts

Primary chondrocytes were derived from P10 mouse tibial growth plates, as described [40]. Briefly, tibial growth plates were dissected and digested in 10 cm plates containing DMEM containing 3 mg/ml Collagenase Type 4

(Worthington Biochemical Corporation, CLS-4) for 90 min in the cell incubator at 37°C. Plates were swirled every 30 min. Following the 90 min, media was replaced with DMEM containing 5 mg/ml Collagenase Type 4 for 3 h in the cell incubator at 37°C. Plates were swirled every 60 min. Media containing digested growth plates was filtered through a 70 mm pore size cell strainer, then centrifuged to pellet the cells. Cells were resuspended in DMEM containing 10% FBS and penicillin/streptomycin and plated.

Primary osteoblasts were derived from P10 mouse calvaria, as described [41]. Briefly, calvaria was dissected in αMEM, rinsed in PBS, then digested in αMEM containing 2 mM L-glutamine and 0.2% collagenase, Type I (Sigma, T1005)/0.05% trypsin (Sigma, C9891) for 20 min in the cell incubator at 37°C. Media from this first digestion was discarded and the calvaria were subjected to an additional four rounds of digestion in αMEM containing 2 mM L-glutamine and 0.2% collagenase, Type I/0.05% trypsin each for 20 min in the cell incubator at 37°C. Following each digestion, media was collected and fetal bovine serum (FBS) was added to obtain 10% final concentration and kept at 4°C. Following the 5th digestion, all media containing digested growth calvaria with 10% FBS was filtered through a 70 mm pore size cell strainer, then centrifuged to pellet the cells. Cells were resuspended in αMEM containing 10% FBS, 2 mM L-glutamine and penicillin/streptomycin, and plated.

Phase-contrast images of primary chondrocytes and osteoblasts were obtained using an EVOS® FL Auto system (ThermoFisher) with an integrated environmental control system (air-CO_2 premix) and CCD monochrome camera.

SAG treatment and qPCR

Confluent cells were treated with 0.1% DMSO or 500 nM SAG for 24 h prior to immunostaining for SMO or for 48 h prior to immersing in Trizol (ThermoFisher) for RNA extraction. Cells were stored in Trizol at −80 °C until RNA extraction. RNA was extracted according to the manufacturer's protocol. One microgram of RNA was converted into cDNA using Quanta Biosciences qScript cDNA mix (VWR International). qPCR was performed in duplicate using Quanta Biosciences Perfecta qPCR Supermix (VWR International) and a BioRad CFX Connect Real-Time PCR Detection System. Primers used were *Thm2* (Forward: 5′-CCC CAC AAT CCA AAC CTA CA-3′; reverse: 5′-GCT CAC AAG CCG ATG GAC-3′); *Gli1* (forward: 5′-CTG ACT GTG CCC GAG AGT G-3′; Reverse: 5′-CGC TGC TGC AAG AGG ACT-3′); m*Gli2* (Forward: 5′ GCA GAC TGC ACC AAG AGG TA 3′; reverse: CGT GGA TGT GTT CAT TGT TGA 3′); m*Gli3* (forward: 5′ CAC CAA AAC AGA ACA CAT TCC A 3′; Reverse: 5′ GGG GTC TGT GTA ACG CTT G 3′) and housekeeping gene m*Oaz1*

(forward: 5′—GCC TGA GGG CAG TAA GGA C-3′; reverse: 5′-GGA GTA GGG CGG CTC TGT-3′).

Osteoblast differentiation assay

Osteoblasts were plated in duplicate into 24-well plates in αMEM containing 10% FBS, 2 mM L-glutamine and penicillin/streptomycin. Upon confluency, cells were cultured in differentiation media, consisting of αMEM, 10% FBS, 2 mM L-glutamine, penicillin/streptomycin and 50 mg/ml ascorbic acid and 5 mM b-glycerophosphate, which was refreshed every 3 days over 2–4 weeks. Cells were fixed with 4% paraformaldehyde for 15 min, then stained with 2% alizarin red solution for 10–15 min in the dark. Once cells reached desired color intensity, cells were washed 4 times with distilled water, then immersed in PBS. Cells were imaged immediately using an EVOS® FL Auto system (ThermoFisher Scientific) with CMOS color camera. Bone nodule formation was quantified as the percentage of the area of redbone nodules/total image area, which were measured using Image J.

Statistics

Unpaired, two-tailed *t* tests for comparison of two groups and one-way ANOVA followed by Tukey's test for comparison of multiple groups were used to evaluate statistical significance ($p < 0.05$) using Graphpad Prism 9.0 software.

Results

THM2 localizes to primary cilia

To characterize the subcellular localization of THM2, an antibody recognizing a unique amino acid sequence encoded within exon 22 was generated (Proteintech). To determine the specificity of the antibody, we generated human embryonic kidney (293 T) *THM2* knock-down (kd) clonal cell lines using lentiviruses expressing *THM2* shRNA. Western blot analysis revealed *THM2* kd, clone 2–1, showed the most effective knockdown (Fig. 1a). We analyzed cilia length in EV 2–5 (empty vector control) and *Thm2* kd 2–1 clonal cell lines by immunostaining for ARL13B, a ciliary membrane marker (Fig. 1b). Quantification of ciliary lengths demonstrated similar lengths between EV and *THM2* kd cell lines (Fig. 1c), indicating THM2 is not required for ciliogenesis. Immunostaining of retinal pigment epithelial (RPE) cells for THM2 showed co-localization with acetylated α-tubulin, a marker of the ciliary axoneme (Fig. 1d), revealing THM2 localizes to primary cilia.

Fig. 1 THM2 is dispensable for ciliogenesis but localizes to the primary cilium. **a** Western blot for THM2 on cellular extracts of 293T EV (control) and *THM2* kd clonal lines. **b** Immunostaining for Arl13B (green) in 293T EV and *THM2* kd (clone 2–1) cells. Scale bar—5 µm. **c** Quantification of cilia lengths. Each data point represents an individual cilium. Graphs represent mean ± SD. **d** Immunostaining for THM2 (green) and acetylated α-tubulin (red) in RPE cells. Scale bar—10 µm
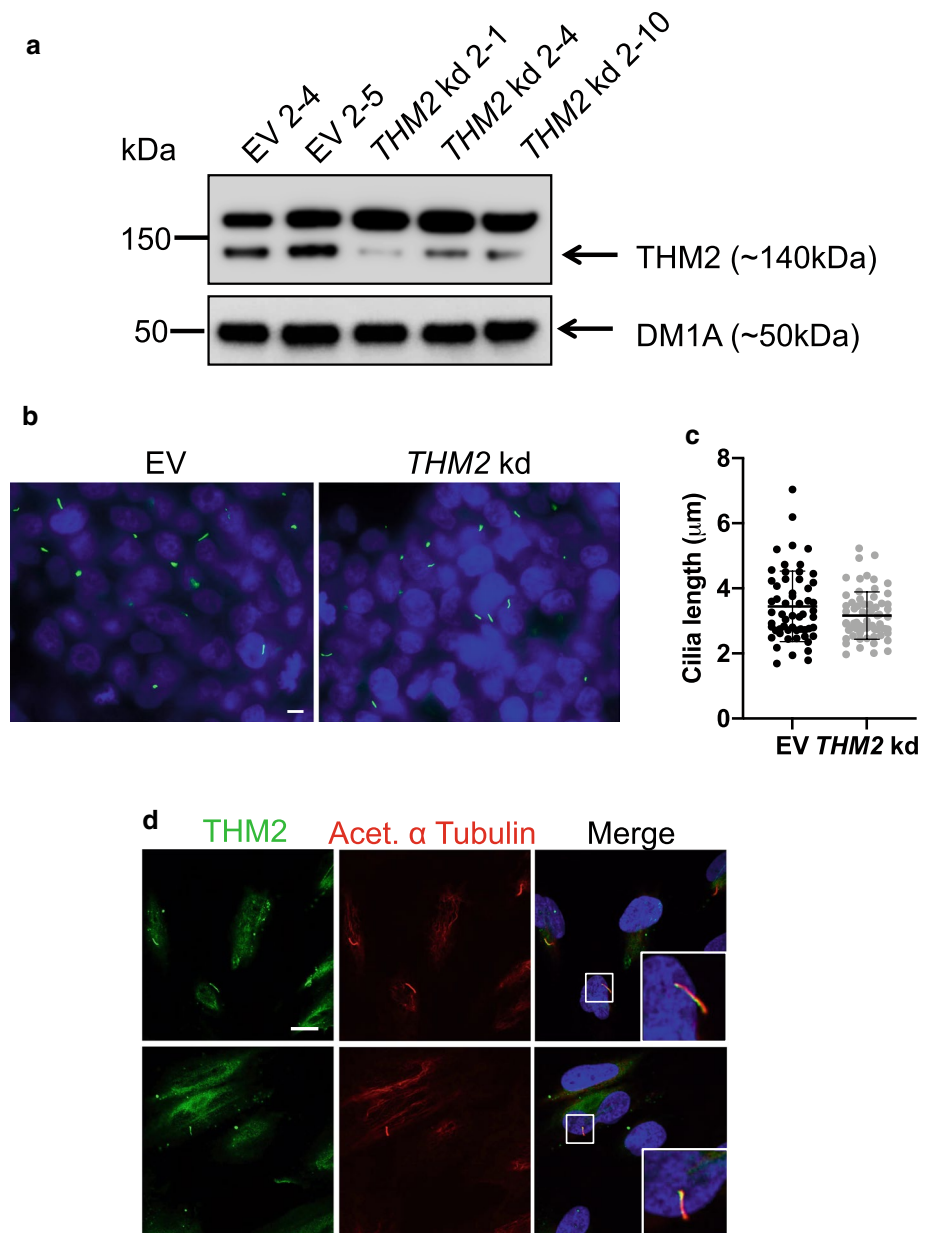

Generation of Thm2 knockout mouse model

Using a *Thm2* knock-out construct from the Knockout Mouse Project (KOMP) repository, we generated a *Thm2* null allele, in which exon 6 was excised, creating a premature stop codon (Fig. 2a). Primers flanking exon 6 were designed to amplify a WT band of 1086 bp and a recombined band at approximately 400 bp (Fig. 2b). Additionally, since this PCR reaction favors amplification of the smaller recombined (*Thm2-null*) allele, we designed additional primers to amplify only the WT allele, generating a 461 bp product. In accordance with the amplification of the mutant band, Western blot analysis confirmed the loss of THM2 protein in testis protein extracts of a *Thm2*-null mouse (Fig. 2c).

Thm2$^{-/-}$; Thm1$^{aln/+}$ mice are smaller than control littermates

Unlike most ciliary gene knock-out mice, which are embryonic lethal [17, 33, 34, 42], *Thm2*-null mice are born, phenotypically indistinguishable from their littermates, and reach adulthood with seemingly normal health. Since paralogs can have redundant functions [43, 44], we introduced a mutant allele of *Thm1 (aln)* onto the *Thm2*-null background. The *aln* allele harbors a missense mutation that results in absence of THM1 protein [17]. We backcrossed the colony five generations onto a C57BL6/J background. At P14, *Thm2$^{-/-}$; Thm1$^{aln/+}$* mice were noticeably smaller than their control littermates with reduced body weight and shorter

Fig. 2 *Thm2* knock-out mouse was generated using a KOMP construct. **a** Schematic diagram of the KOMP constructs in genomic DNA of *Thm2*. Exons are represented by black boxes and introns by the black line. Lox P sites surrounding exon 6 are depicted as red triangles. Genomic primers are indicated in blue (WT and recombination band) and purple (WT band). Splicing of exon 6 creates a premature stop codon. **b** PCR analysis of WT, *Thm2*$^{+/-}$, and *Thm2*$^{-/-}$ genotypes using primers indicated in the blue and additional confirmation of the WT allele in WT and *Thm2*$^{+/-}$ mice using primers indicated in purple. **c** Western blot analysis of P14 testis extracts confirms the loss of THM2 in *Thm2* ko mice
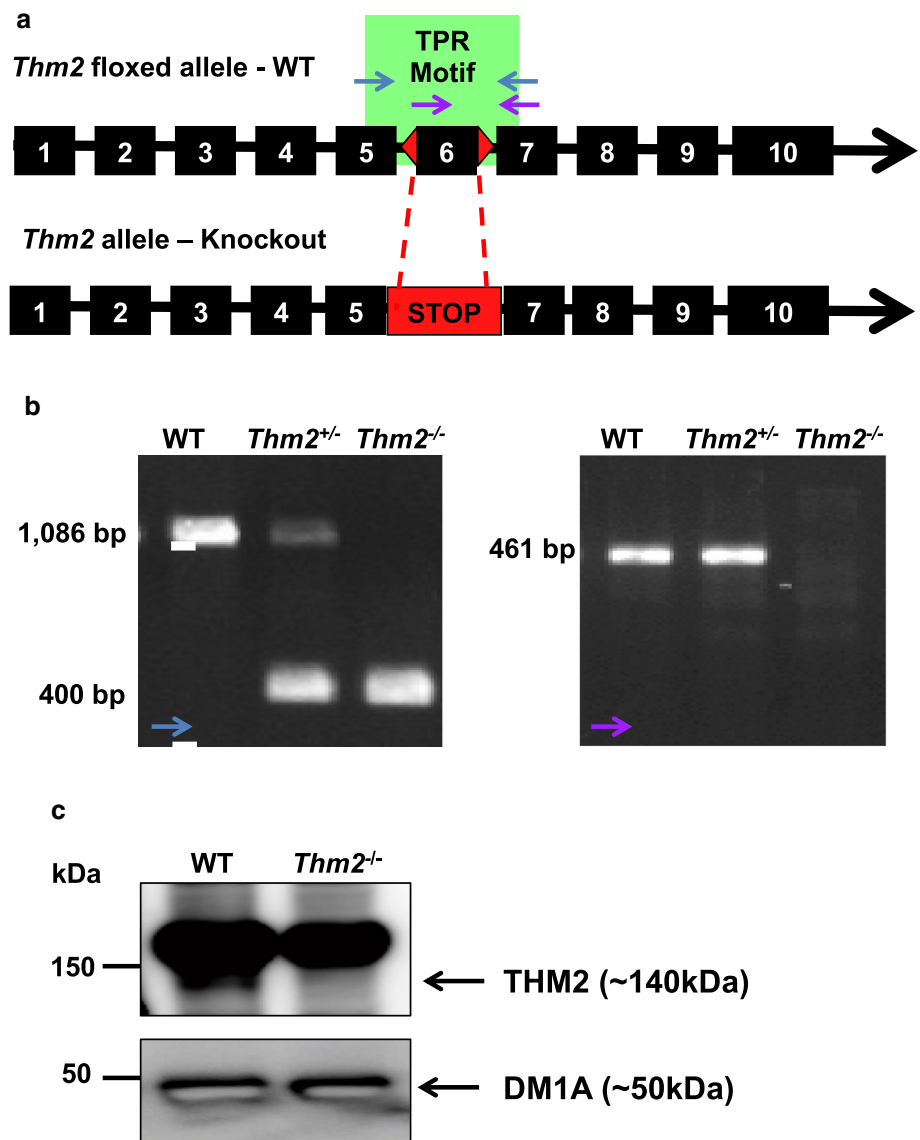
crown-to-rump length (Fig. 3a, b). This phenotype was also observed at P21 (Fig. 3c), and we noted that a proportion of triple allele mutant mice (7/25 = 28%) do not survive to weaning age.

Thm2$^{-/-}$; *Thm1*$^{aln/+}$ lung weight/body weight ratio is increased

Since renal cysts are among the most common clinical manifestations of ciliopathies [3], we analyzed the kidneys of P14 *Thm2*$^{-/-}$; *Thm1*$^{aln/+}$ mice. Histological analysis revealed normal kidney morphology of *Thm2*$^{-/-}$; *Thm1*$^{aln/+}$ mice (Fig. 4a). Total kidney weights were smaller in *Thm2*$^{-/-}$; *Thm1*$^{aln/+}$ mice, but this was proportional to body size since kidney weight/body weight ratios of *Thm2*$^{-/-}$; *Thm1*$^{aln/+}$ mice were similar to those of control littermates. Similarly, heart weight was lower in triple allele mutant mice, but heart

weight/body weight ratios were comparable between control and *Thm2*$^{-/-}$; *Thm1*$^{aln/+}$ mice (Fig. 4b). In contrast, although lung weight was lower in triple allele mutant mice, lung weight/body weight ratio was elevated in triple allele mutant mice relative to control mice (Fig. 4c).

Thm2$^{-/-}$;*Thm1*$^{aln/+}$ mice exhibit shortened and less dense bone

We next performed skeletal preparations to examine the skeletal phenotype of *Thm2*$^{-/-}$; *Thm1*$^{aln/+}$ mice (Fig. 5a). At P14, *Thm2*$^{-/-}$; *Thm1*$^{aln/+}$ mice exhibited shorter long bones, including tibia, femur, humerus, radius and ulna (Fig. 5b). The sternum and ribcage diameter of *Thm2*$^{-/-}$; *Thm1*$^{aln/+}$ mice were also smaller than those of control littermates. Additionally, cranial length, as measured from the tip of the nose to back of the head, was shorter in

Fig. 3 *Thm2⁻/⁻; Thm1ᵃˡⁿ/⁺* mice exhibit a runted phenotype. Following five generations of backcrossing onto a C57BL6/J background, triple allele mutants showed a runted phenotype. **a** Images of mice at P14. **b** Body weights and crown-to-rump lengths at P14 and **c** at P21. Error bars represent mean ± SD. Statistical significance was determined using one-way ANOVA and Tukey's test. ****$p < 0.0001$
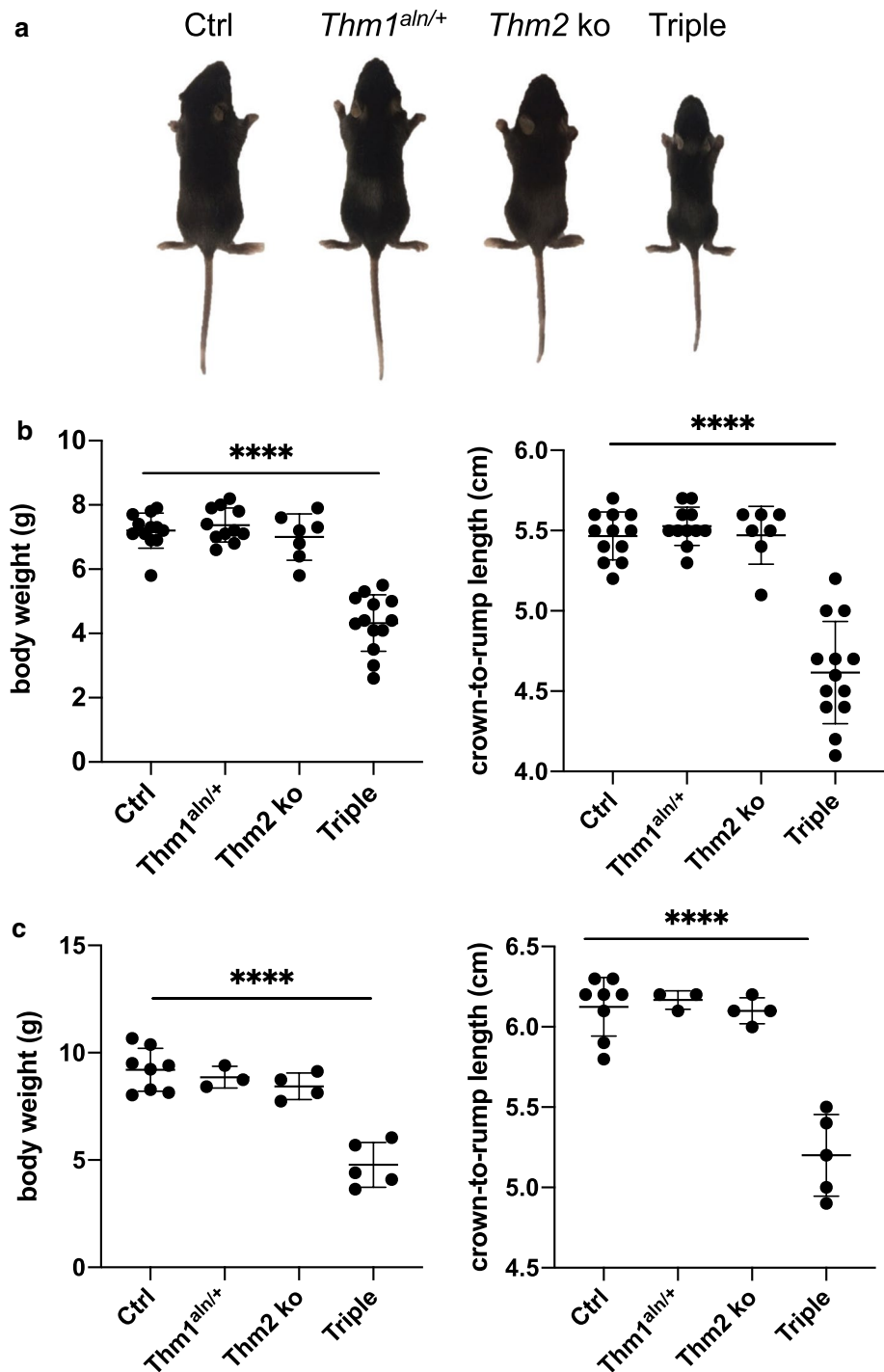

Thm2⁻/⁻; Thm1ᵃˡⁿ/⁺ mice. To determine if these reduced bone lengths reflect the overall dwarfing of the tripe allele mutants, we examined bone length/crown-to-rump length ratios. Long bone, sternum and ribcage/crown-to-rump ratios were similar between control and triple allele mutants, but the skull/crown-to-rump ratio was slightly increased in triple allele mutants (Fig. 5c). Moreover, triple allele mutants showed small mandible/skull ratios, indicative of craniofacial defects (Fig. 5d).

We further analyzed the *Thm2⁻/⁻; Thm1ᵃˡⁿ/⁺* skeleton using radiography (Fig. 6a and b). Individual caudal vertebra length was decreased in *Thm2⁻/⁻; Thm1ᵃˡⁿ/⁺* mice

Fig. 4 *Thm2⁻/⁻; Thm1ᵃˡⁿ/⁺* mice have increased lung/body-weight ratios. **a** Haematoxylin and eosin staining of kidney sections from P14 mice. Scale bars—1 mm and 500 μm, upper and lower panels. Two kidney weights and % kidney weight/body weight ratios. **b** Heart weights and % heart weight/body weight ratios. **c** Lung weights and % heart weight/body weight ratios. Graphs represent mean ± SD. Statistical significance was determined using one-way ANOVA and Tukey's test. *$p < 0.05$; **$p < 0.005$
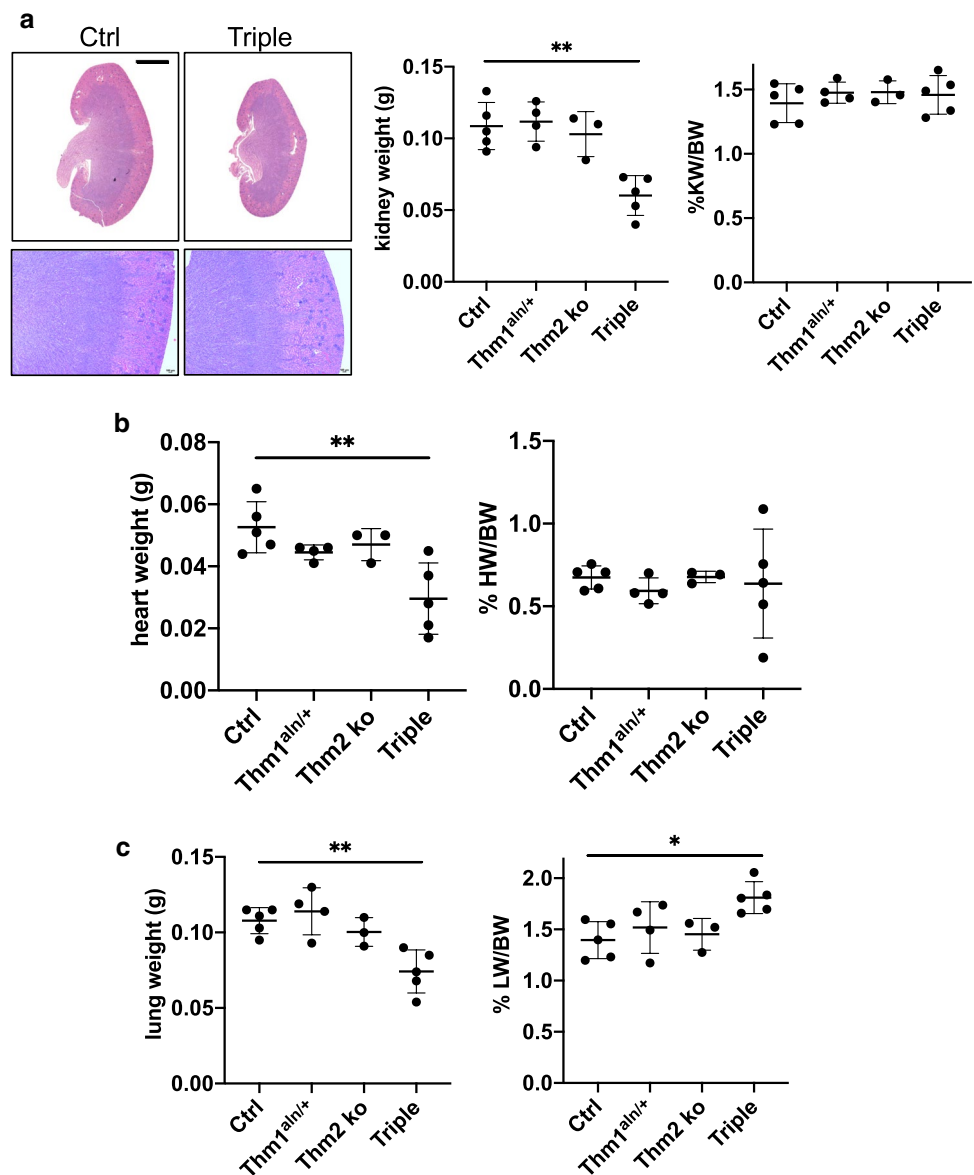
(Fig. 6c), but in proportion to crown-to-rump length (Fig. 6d). We also noted that the hindlimb and tibia of *Thm2⁻/⁻; Thm1ᵃˡⁿ/⁺* mice were less opaque than those of control mice using both radiography and micro-computed topography (Fig. 6e and f). This was particularly noticeable when tibias were rotated (Movies S1 and S2). Consistent with this, *Thm2⁻/⁻; Thm1ᵃˡⁿ/⁺* tibia showed reduced cortical bone mineral density (BMD), cortical thickness, and cortical bone area at mid-diaphysis and proximal end of the tibia (Figs. 6g-6h). Additionally, cortical area fraction (cortical bone area/total area) at the proximal end of the tibia, as well as trabecular BMD were reduced (Fig. 6i, j). Other cortical and trabecular bone properties of control and *Thm2⁻/⁻; Thm1ᵃˡⁿ/⁺* tibia were similar (Fig. S1).

These data demonstrate that *Thm2*, together with *Thm1*, is required for postnatal skeletal growth.

Growth plates of Thm2⁻/⁻;Thm1ᵃˡⁿ/⁺ show aberrant architecture

To determine the cause of the tibial skeletal defects, we next examined chondrocyte organization in the tibial growth plate. Broadly, the growth plate can be divided into two major regions: the proliferative zone and the hypertrophic zone [45]. As part of endochondral ossification, chondrocyte differentiation occurs. In this process, early chondroblasts are stimulated to proliferate, then become pre-hypertrophic, hypertrophic, and finally undergo cell death and calcification of cartilage. Capillaries and
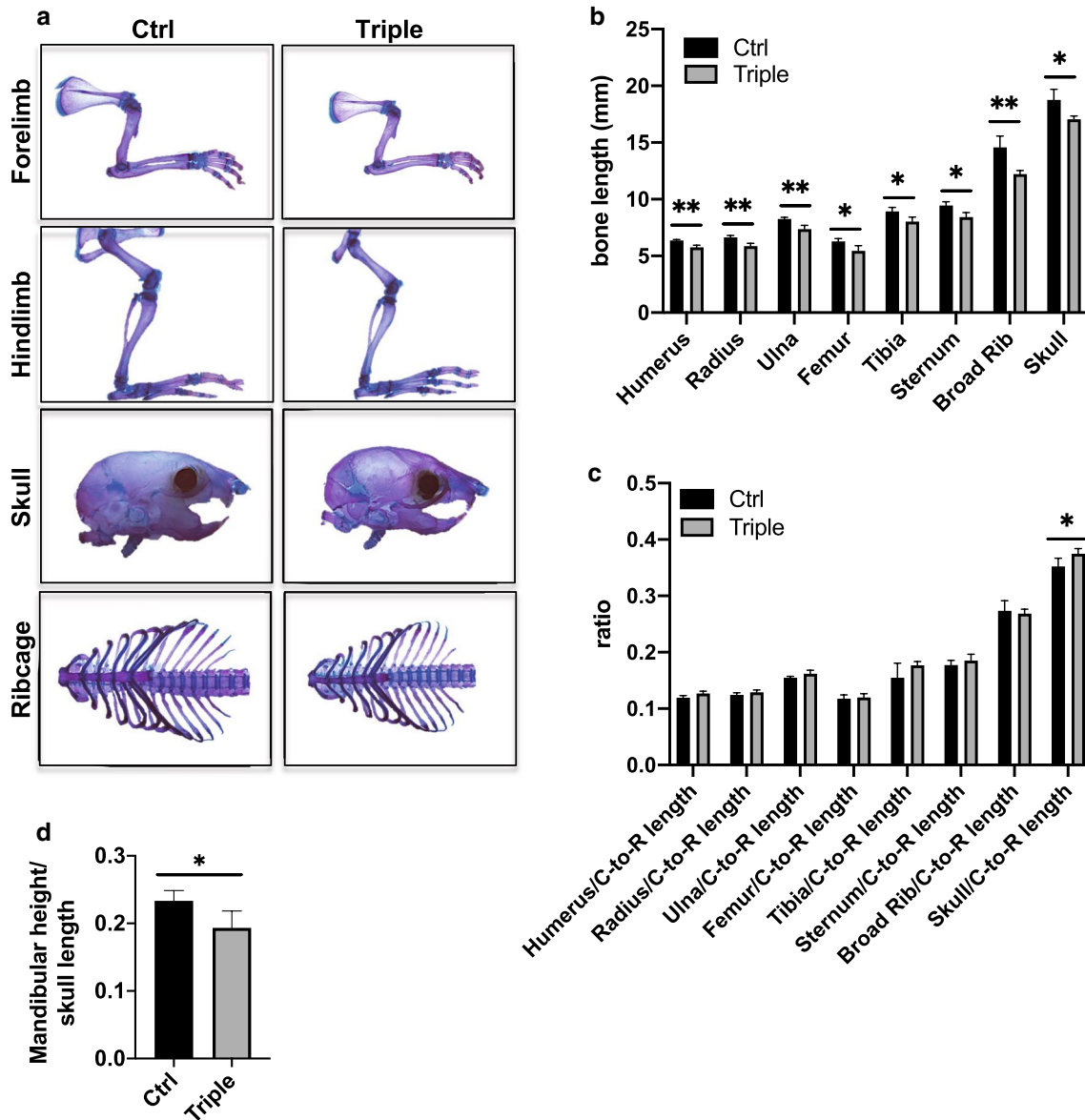
Fig. 5 *Thm2⁻/⁻; Thm1ᵃˡⁿ/⁺* mice have shorter bones. **a** Skeletal preparations at P14 using alizarin red (bone) and alcian blue staining (cartilage). **b** Bone lengths. **c** Bone/Crown-to-Rump (C-to-R) length ratios. **d** Mandibular height/cranial length. Graphs represent mean ± SD of $n = 4$ ctrl and $n = 4$ triple allele mutant mice. Statistical significance was determined using two-tailed, unpaired t test. *$p < 0.05$; **$p < 0.005$

osteoblasts invade the cartilage matrix and form new bone which replaces cartilage. H&E staining, as well as Safranin O and fast green staining, which marks cartilage and bone, respectively, of P14 *Thm2⁻/⁻; Thm1ᵃˡⁿ/⁺* tibial growth plates revealed an expanded proliferation zone and a reduced hypertrophic zone (Fig. 7). We also observed a more basophilic H&E staining and more intense safranin-O staining in the *Thm2⁻/⁻; Thm1ᵃˡⁿ/⁺* growth plate cartilage proliferation zone. This may indicate a change in the

proteoglycan content of the extracellular matrix. Together, these defects suggest impaired chondrocyte hypertrophy and endochondral ossification, which could contribute to the shortened long bones seen in *Thm2⁻/⁻; Thm1ᵃˡⁿ/⁺ mice*.

Thm2⁻/⁻; Thm1ᵃˡⁿ/⁺ chondrocytes show increased Hh response

Chondrocyte differentiation in the growth plate is regulated by ciliary-mediated canonical Hedgehog (Hh) signaling [46]. We, therefore, examined primary cilia and Hh signaling in triple allele mutant chondrocytes. Immunostaining for the ciliary marker, Arl13B, on chondrocytes of the growth plate suggested similar ciliary lengths between control and *Thm2⁻/⁻; Thm1ᵃˡⁿ/⁺* tissue (Fig. 8a). Incorporation of a *Gli1-lacZ* allele, which acts as a reporter of the Hh pathway, revealed increased *Gli1* expression in chondrocytes of the triple allele mutant growth plate (Figs. 8b and c). To further examine Hh signaling, we generated primary chondrocytes from P10 tibial growth plates (Fig. 8d). Cilia lengths were similar between control and triple allele mutant primary cells (Fig. 8e, f). In response to Hh stimulation, the Smoothened (SMO) signal transducer translocates to the primary cilium [12]. Accordingly, treatment of cells with Smoothened Agonist (SAG) caused the enrichment of SMO in cilia (Fig. 8g). SAG-induced increase in ciliary SMO was similar between control and triple allele mutant chondrocytes (Fig. 8h). qPCR revealed reduced *Thm2* transcripts in triple allele mutant cells (Fig. 8i). In both control and triple allele mutant chondrocytes, SAG treatment caused an increase in *Gli1* and *Gli2* transcripts and did not affect *Gli3* (Fig. 8j–l). However, SAG induced a greater increase in *Gli1* transcription in triple allele mutant chondrocytes relative to control cells, suggesting the triple allele mutation causes an increased Hh response in chondrocytes.

Reducing Gli2 dosage in Thm2-null mice results in a small phenotype

To determine whether Hh signaling contributes to the skeletal phenotype, we introduced a null allele of *Gli2*, the main transcriptional activator of the Hh pathway, into the *Thm2; Thm1* colony. Since chondrocytes show an elevated Hh response, we anticipated that reducing Hh signaling would correct the runted phenotype. While *Gli2⁻/⁻* mice show skeletal defects and perinatal lethality, the *Gli2±* genotype does not result in a phenotype [47]. Yet the loss of one allele of *Gli2* in *Thm2⁻/⁻; Thm1ᵃˡⁿ/⁺; Gli2⁺/⁻* mice further decreased body weight and crown-to-rump length relative to triple allele mutant mice (Fig. 9a–c). Additionally, loss of one allele of *Gli2* in *Thm2⁻/⁻; Gli2⁺/⁻* mice resulted in a small phenotype, with reduced body weight and crown-to-rump length relative to control and *Thm2⁻/⁻* mice. Thus, reducing Hh signaling uncovers a role for *Thm2* in postnatal skeletal growth. Further, the exacerbated runted phenotype of triple allele mutants by *Gli2* deficiency could suggest that *Thm2,*

together with *Thm1,* positively regulates the Hh pathway in cells that are not chondrocytes.

Thm2⁻/⁻; Thm1ᵃˡⁿ/⁺ osteoblasts show defective differentiation

We, therefore, derived primary osteoblasts from calvaria of P10 mice (Fig. 10a). We immunostained osteoblasts for primary cilia (Fig. 10b), which revealed similar cilia lengths between control and mutant osteoblasts (Fig. 10c). SAG treatment resulted in normal ciliary localization of SMO in mutant osteoblasts (Fig. 10d, e). qPCR showed reduced *Thm2* transcripts in triple allele mutant osteoblasts (Fig. 10f). SAG treatment-induced increases in *Gli1* transcripts that were similar between control and mutant osteoblasts (Fig. 10g), while *Gli2* and *Gli3* transcripts were not altered (Fig. 10h, i). However, the formation of bone nodules by the triple allele mutant osteoblasts was markedly impaired (Fig. 10j, k), indicating the triple allele mutation impairs differentiation of osteoblasts.

Discussion

This study establishes THM2 as a ciliary protein. *Thm2* depletion results in normal cilia length, but the loss of *Thm2,* together with loss of one allele of either *Thm1* or *Gli2,* impairs postnatal skeletal growth, resulting in a small phenotype. The small phenotype in *Thm2⁻/⁻; Thm1ᵃˡⁿ/⁺* mouse mutants is accompanied by small mandible and architectural defects of the long bone (tibia), including decreased bone mineral density. Additionally, the *Thm2⁻/⁻; Thm1ᵃˡⁿ/⁺* genetic interaction is important for both chondrocyte and osteoblast differentiation, and for negative regulation of Hh signaling downstream of SMO ciliary localization in chondrocytes. Our findings expand the IFT genes and genetic network that regulate skeletal development. The *Thm2⁻/⁻; Thm1ᵃˡⁿ/⁺* mouse is also the first global *Ift*-null mouse model surviving embryogenesis and exhibiting postnatal skeletal abnormalities.

Although *Thm2* and *Thm1* genetically interact in skeletal development, notably, the skeletal and ciliary phenotypes differ between *Thm1ᵃˡⁿ/ᵃˡⁿ* and *Thm2⁻/⁻; Thm1ᵃˡⁿ/⁺* mouse mutants. The *Thm1ᵃˡⁿ/ᵃˡⁿ* mouse mutant exhibits shortened long bones and ribs, with normal crown-to-rump length [32]. Additionally, mutations in *THM1* have been identified in patients with Jeune Syndrome, a skeletal ciliopathy characterized by shortened long bones and ribs relative to body trunk length [18]. In contrast to this disproportionate dwarfism, the *Thm2⁻/⁻; Thm1ᵃˡⁿ/⁺* mice are small in stature overall. There are other IFT mouse mutants that also display an overall runted phenotype.

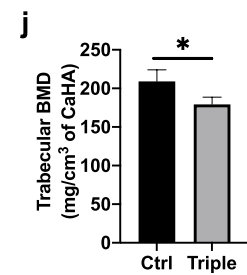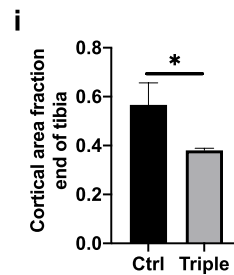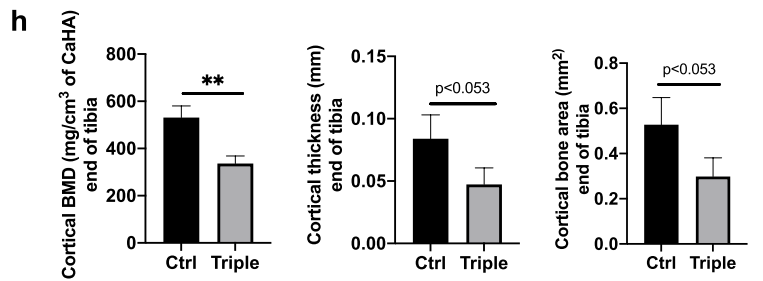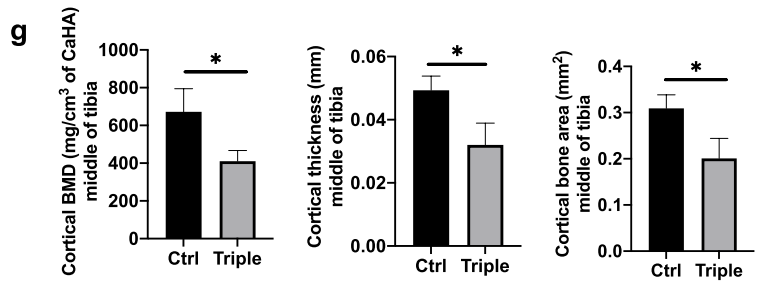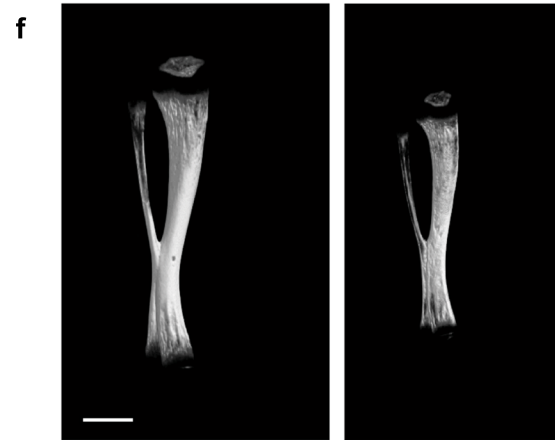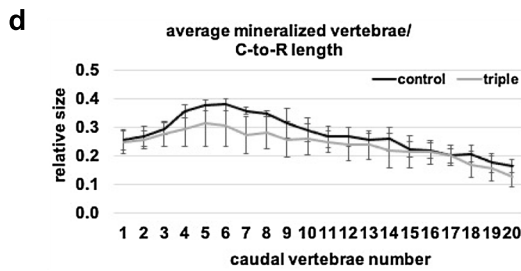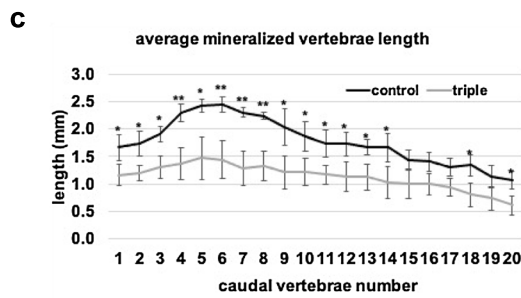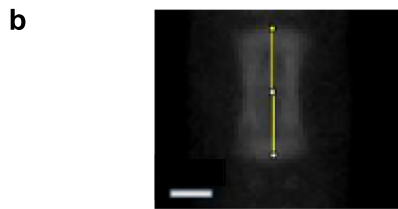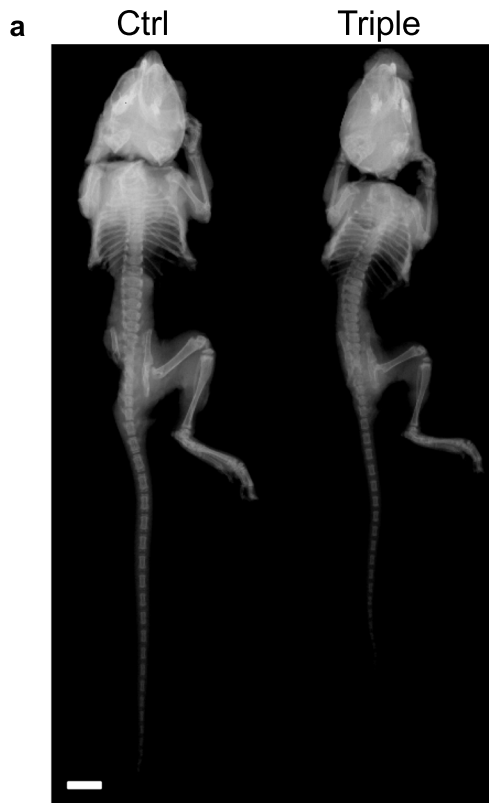◄**Fig. 6** *Thm2⁻/⁻; Thm1ᵃˡⁿ/⁺* tibia have less dense bone. **a** Radiographs of P14 skeleton and **b** vertebra. Scale bars—1 cm and 500 μm, respectively. **c** Caudal vertebrae lengths by number. **d** Caudal vertebrae/Crown-to-Rump (C-to-R) length ratios. Graphs represent mean ± SD of $n = 3$ ctrl and $n = 3$ triple allele mutant mice. Statistical significance was determined using two-tailed, unpaired t-test. $*p < 0.05$; $**p < 0.01$ **e** Radiographs of hindlimbs and **f** microCT imaging of tibias. Scale bars—5 mm and 1 mm, respectively. **g** Cortical bone mineral density (BMD), thickness and area at mid-diaphysis and **h** at the proximal end of tibia. **i** Cortical bone area/total bone area (fraction) at the proximal end of tibia. **j** Trabecular BMD at proximal end of tibia. Graphs represent mean ± SD of $n = 3$ ctrl and $n = 3$ triple allele mutant mice. Statistical significance was determined using a two-tailed, unpaired *t* test. $*p < 0.05$; $**p < 0.005$

This includes the *Ift140* conditional knock-out mouse, in which *Ift140* is deleted in osteoblasts using the *Osx*-Cre [48]. Additionally, *Ift80ᵍᵗ/ᵍᵗ* hypomorphic mutant mice are also small in stature [35]. Proportionately small mice may reflect that the mutation affects the growth of most or all bones, instead of primarily affecting the long bones and ribs. In the human population, proportionate dwarfism causes small stature. In patients with proportionate dwarfism, mutations have been identified in centriole-related genes, such as pericentrin [49], *CEP152* [50], and *CENPJ4* [51]. Interestingly, defects in centriolar satellites have been observed in cells depleted of certain IFT-A subunits [52], raising the possibility that a centriole-related component might also be defective in the small IFT mouse mutants and thus may warrant investigation.

Further contrasting with *Thm1ᵃˡⁿ/ᵃˡⁿ* mouse embryos [17, 32], *Thm2⁻/⁻; Thm1ᵃˡⁿ/⁺* mice are not polydyactylous. Preaxial polydactyly is caused by disrupted GLI3A:GLI3R ratios along the anterior–posterior axis of the developing limb bud [53]. Since *Thm2* and *Thm1* show very similar expression patterns in E10.5 whole-mount mouse embryos [17], the absence of polydactyly in *Thm2⁻/⁻; Thm1ᵃˡⁿ/⁺* mice indicates divergent mechanisms of Hh regulation between the *Thm2;Thm1* genetic interaction and *Thm1* alone. *Thm1* loss disrupts GLI3 processing [17], while the *Thm2⁻/⁻; Thm1ᵃˡⁿ/⁺* mutation likely does not. Finally, while *Thm2⁻/⁻; Thm1ᵃˡⁿ/⁺* cilia lengths and kidneys appear normal, loss of *Thm1* causes shortened primary cilia with a bulbous distal tip and cystic kidneys [54]. Together, these differences reflect the unique and redundant roles of the *Thm1* and *Thm2* paralogs.

In the growth plate, Parathyroid hormone-related protein (PTHrP) is expressed by perichondral cells and chondrocytes to promote chondrocyte proliferation [45]. When PTHrP levels reach below a certain threshold, pre-hypertrophic and early hypertrophic cells produce *Indian Hedgehog* (*Ihh*), which effects various skeletal processes, including increased chondrocyte proliferation, stimulation of PTHrP production, and differentiation of perichondral cells to osteoblasts of the bone collar [45]. In E14.5 *Ihh*-null mice, Hh signaling is decreased in growth plates and the proliferation zone is reduced [55]. Conversely, in mice harboring a *Col2a1*-specific knock-out of *Suppressor of Fused* (*Sufu*), a negative regulator of Hh signaling, Hh signaling is increased in growth plates, causing an increased proliferation zone and a reduced hypertrophic zone [56]. Similarly, in triple allele mutant growth plates, Hh signaling is increased in chondrocytes, and the proliferation zone is increased while the hypertrophic zone is reduced. Thus, deficiency of Hh signaling causes chondrocytes to undergo premature hypertrophy, while inappropriate activation of Hh signaling causes chondrocytes to remain in the proliferation zone[57]. Both alterations impair endochondral bone formation.

In triple allele mutant osteoblasts, a defect in Hh response to (500 nM) SAG was not observed. The differential Hh response in chondrocytes and osteoblasts indicates cell-specific regulation of Hh signaling by the triple allele mutation. Cell-specific Hh regulation by *Thm1* and other ciliary genes has been reported [17, 20, 58]. In other experiments, we have observed that SAG-treated *Thm2⁻/⁻* mouse embryonic fibroblasts (MEF) have normal SMO ciliary localization and *Gli1* transcription, while SAG-treated triple allele mutant MEF shows normal SMO ciliary localization but reduced *Gli1* transcription [59]. Collectively, our data suggest that the triple allele mutation alters Hh signaling in a cell-specific manner, downstream of SMO ciliary localization, possibly at the level of SMO or GLI activation.

Although a defect in Hh signaling was not detected in triple allele mutant primary osteoblasts, in vitro differentiation was impaired. This could indicate two possibilities: (1) that the in vitro Hh assays were not sensitive enough to detect a more subtle Hh signaling defect and/or (2) that another signaling pathway is perturbed. Misregulation of several pathways, including TGF-β, Notch and Wnt, hampers in vitro bone nodule formation, and knockout mice of components of these pathways exhibit skeletal defects [41, 60–63]. Thus, future experiments will examine these two possibilities. Since *Gli2* deficiency in the triple allele mutant exacerbated the runted phenotype, rather than rescuing it, we propose that the chondrocyte defect may be superseded by the osteoblast defect in this global knock-out. In endochondral ossification, osteoblasts act downstream of chondrocytes, replacing the extracellular matrix laid down by the chondrocytes with bone. Additionally, deletion of IFT-A gene, *Ift140,* in osteoblasts causes a small phenotype [48], demonstrating that loss of an IFT gene in osteoblasts can
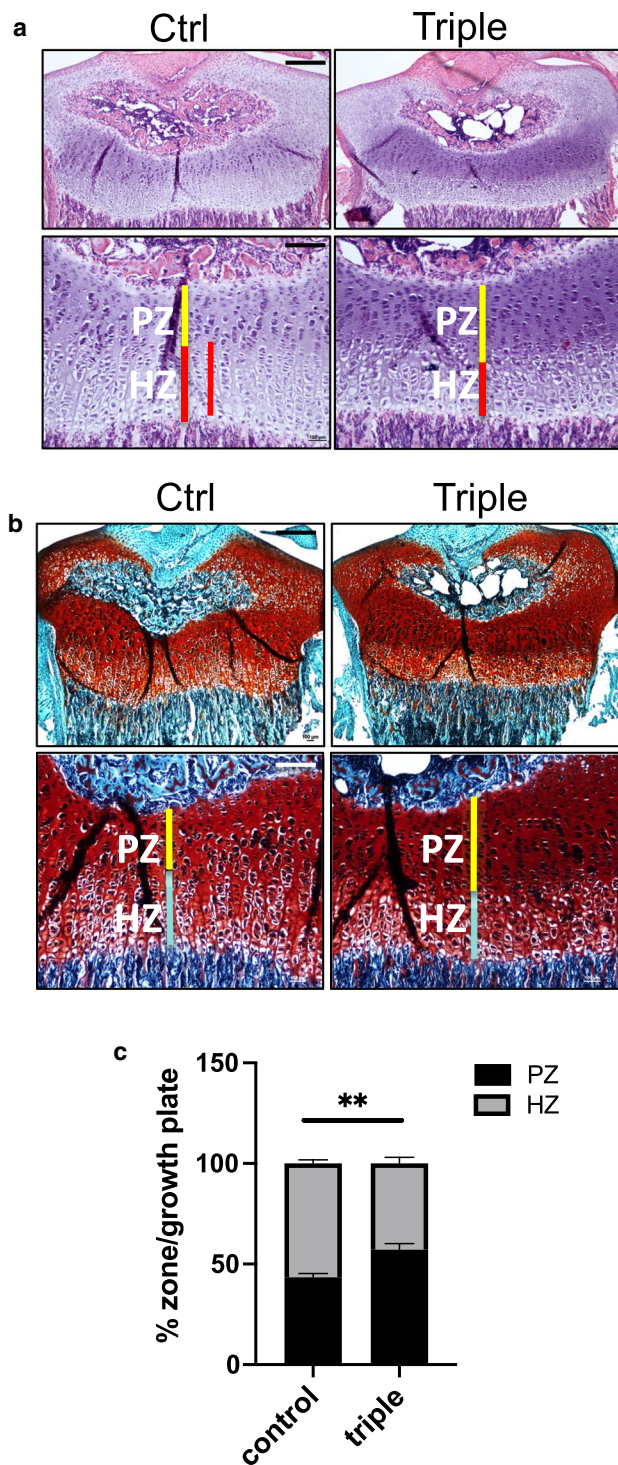
Fig. 7 $Thm2^{-/-}$; $Thm1^{aln/+}$ mice have altered tibial growth plates. **a** Haematoxylin and eosin (H&E) and **b** Safranin O and fast green staining of growth plates at P14. Scale bars—500 μm and 200 μm, upper and lower panels. PZ - proliferation zone, HZ - hypertropic zone **c** Quantification of % PZ/growth plate and % HZ/growth plate from H&E images. Error bars represent SD of $n=3$ ctrl and $n=3$ triple allele mutant growth plates. Statistical significance was determined using two-tailed, unpaired t test. **$p \leq 0.005$

result in small stature. Since the loss of just one allele of *Gli2* is sufficient to worsen the triple allele mutant small phenotype, we propose that the altered pathway in osteoblasts may potentially interact with *Gli2*.

Skeletal ciliopathies manifest varying degrees of severity, and this characteristic is present in triple allele mutant mice, in which almost a third of triple allele mutants do not survive to weaning. In addition to levels of *Gli2*, genetic background modifies the triple allele mutant small phenotype, since the phenotype was apparent only once the colony was backcrossed from a mixed FVB/C57BL6/J strain background to C57BL6/J over five generations. Taken together, cell type, genetic interaction, and strain background are important determinants of cilia dysfunction and ciliopathy phenotypes. Additionally, the mechanisms by which ciliary defects cause developmental defects can differ due to variations in the function of individual ciliary proteins. For example, germline deletion of almost all reported *Ift* genes causes misregulation of the Hh pathway, but not all *Ift* gene deletions affect ciliary structure [11, 64].

Direct evidence of a ciliopathy in $Thm2^{-/-}$; $Thm1^{aln/+}$ mice is still lacking. Finding a ciliary defect (structural and/or ciliary mislocalization of proteins) may require high-resolution imaging. For instance, $Ift25^{-/-}$ cilia appear normal using conventional fluorescence microscopy [64] but show abnormal structure using super-resolution microscopy [65]. Additionally, $Ift56^{hop/hop}$ cilia also appear grossly normal but have defects of the axonemal microtubules revealed by transmission electron microscopy [66]. Alternatively, *Thm2* together with *Thm1* may play a role outside the cilium. Future experiments will explore both possibilities.

Thm2 is the least explored IFT gene, but roles for THM2 are emerging. Mutations in *THM2* have been identified in male patients with infertility [38]. In contrast, our $Thm2^{-/-}$ mice do not show evidence of fertility defects, which could suggest there is redundancy in the mouse or that *Thm2* functions as part of a genetic network to regulate fertility. Other studies also suggest that *THM2* expression may be misregulated in certain cancers and in neuronal degeneration [67–69]. For the first time, our study shows that THM2 can localize to primary cilia and that *Thm2* regulates postnatal skeletal development. Thus, *THM2* could be an additional locus to query in patients with skeletal dysplasia. This work generates the first global IFT gene knock-out mouse that allows the study of skeletal development postnatally. This model will enable future biomechanical studies, including identification of mechanical or chemical stimuli that are received and transduced by primary cilia to regulate bone development and homeostasis.
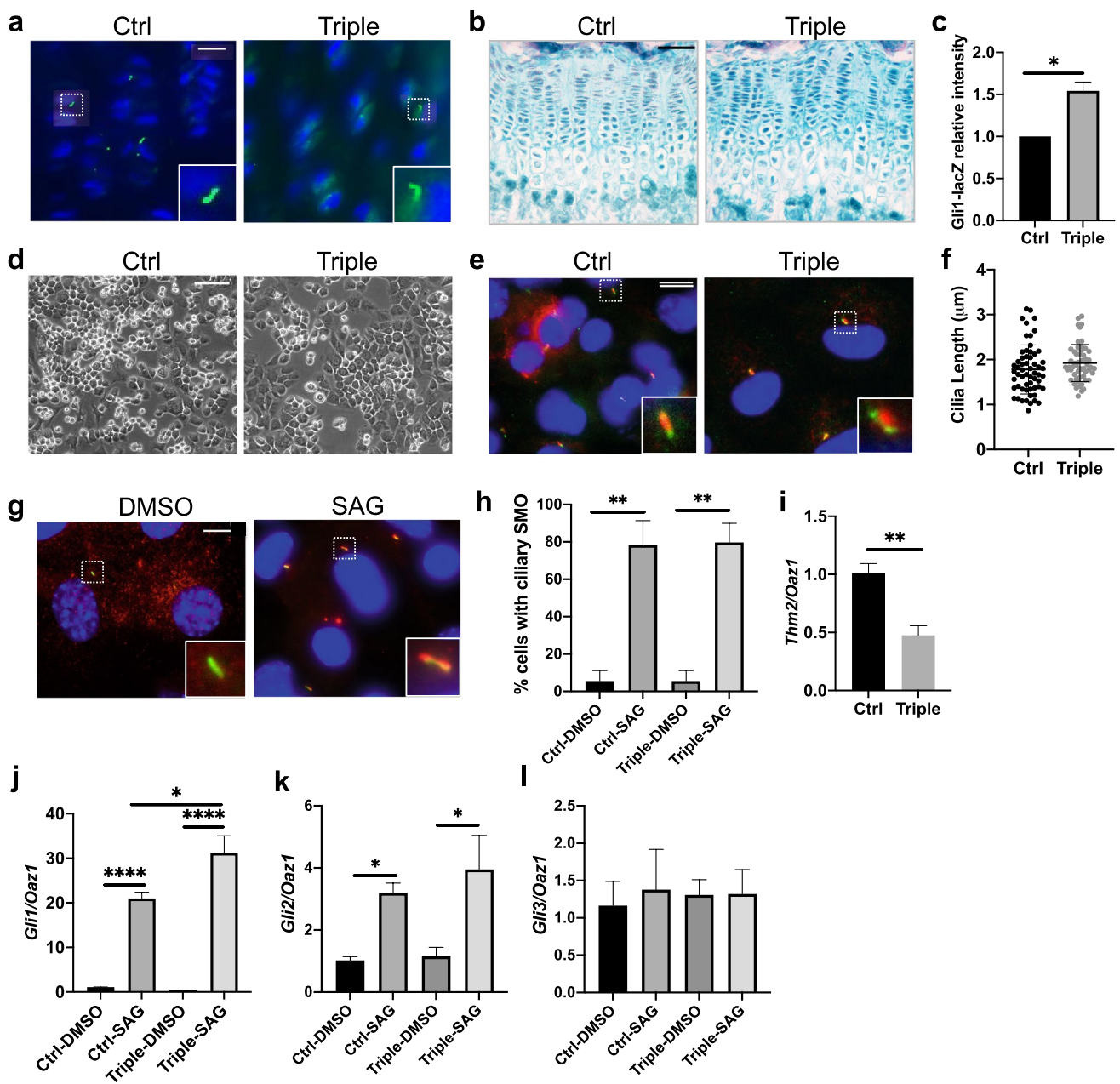
Fig. 8 Hedgehog signaling is increased in *Thm2^{-/-}; Thm1^{aln/+}* chondrocytes. **a** Immunostaining of P14 tibial growth plates for ciliary membrane marker, Arl13B (green). Scale bar—10 μm. **b** Gli-lacZ staining of growth plates. Scale bar—100 μm. **c** Quantification of Gli1-lacZ staining. Error bars represent mean ± SEM from n = 4 ctrl and n = 5 triple allele mutant mice. **d** Phase contrast images of tibial growth plate-derived primary chondrocytes. Scale bar—100 μm. **e** Immunostaining for ciliary markers, acetylated α-tubulin (red) and IFT81 (green). Scale bar—10 μm. **f** Quantification of ciliary lengths. Error bars represent mean ± SD from n = 3 ctrl and n = 3 triple allele mutant mice. **g** Ciliary localization of SMO (red) and ARL13B (green) in response to vehicle (DMSO) or SAG. Scale bar—10 μm. **h** Quantification of percentage of cells with ciliary SMO **i** qPCR for *Thm2*; **j** *Gli1*; **k** *Gli2*; and **l** *Gli3* relative to *Oaz1*. Bar graphs represent mean ± SEM from cell cultures of n = 4 ctrl and n = 4 triple allele mutant mice. Statistical significance was determined using unpaired t test for **c** and **i** and one-way ANOVA and Tukey's test for **h–l**. *p < 0.05; **p < 0.01, ****p < 0.001

Fig. 9 *Gli2* deficiency causes small phenotype in *Thm2* ko mice and exacerbates small phenotype in *Thm2⁻/⁻; Thm1ᵃˡⁿ/⁺* mice. **a** Images of P14 littermates. **b** Body weight and crown-to-rump lengths at P14 and **c** at P21. Graphs represent mean ± SD. Statistical significance was determined using one-way ANOVA and Tukey's test. $^{\#}p<0.05$; $^{\#\#}p<0.01$; $^{\#\#\#}p<0.005$; $^{\#\#\#\#}p<0.0001$ relative to Ctrl. $^{*}p<0.05$
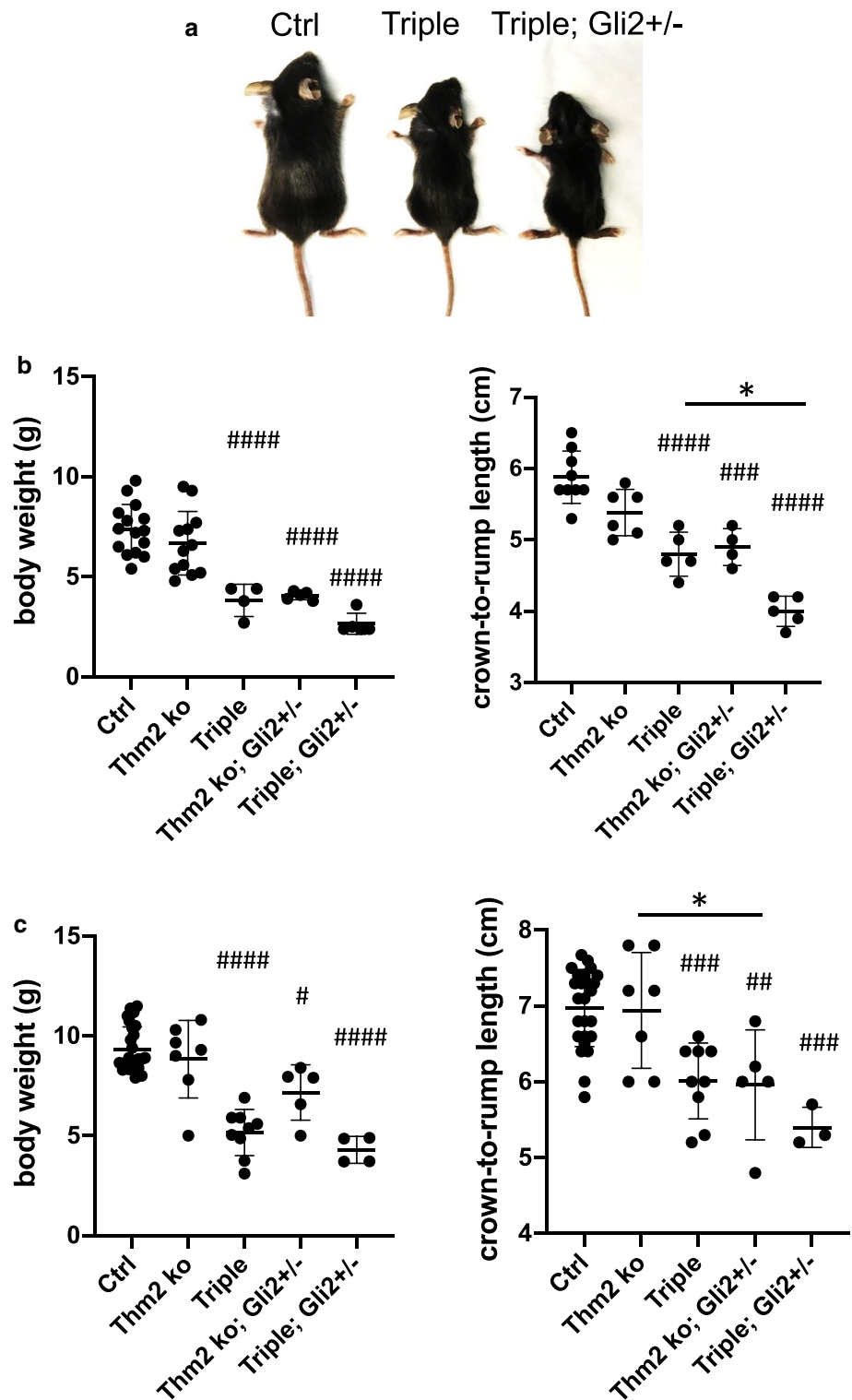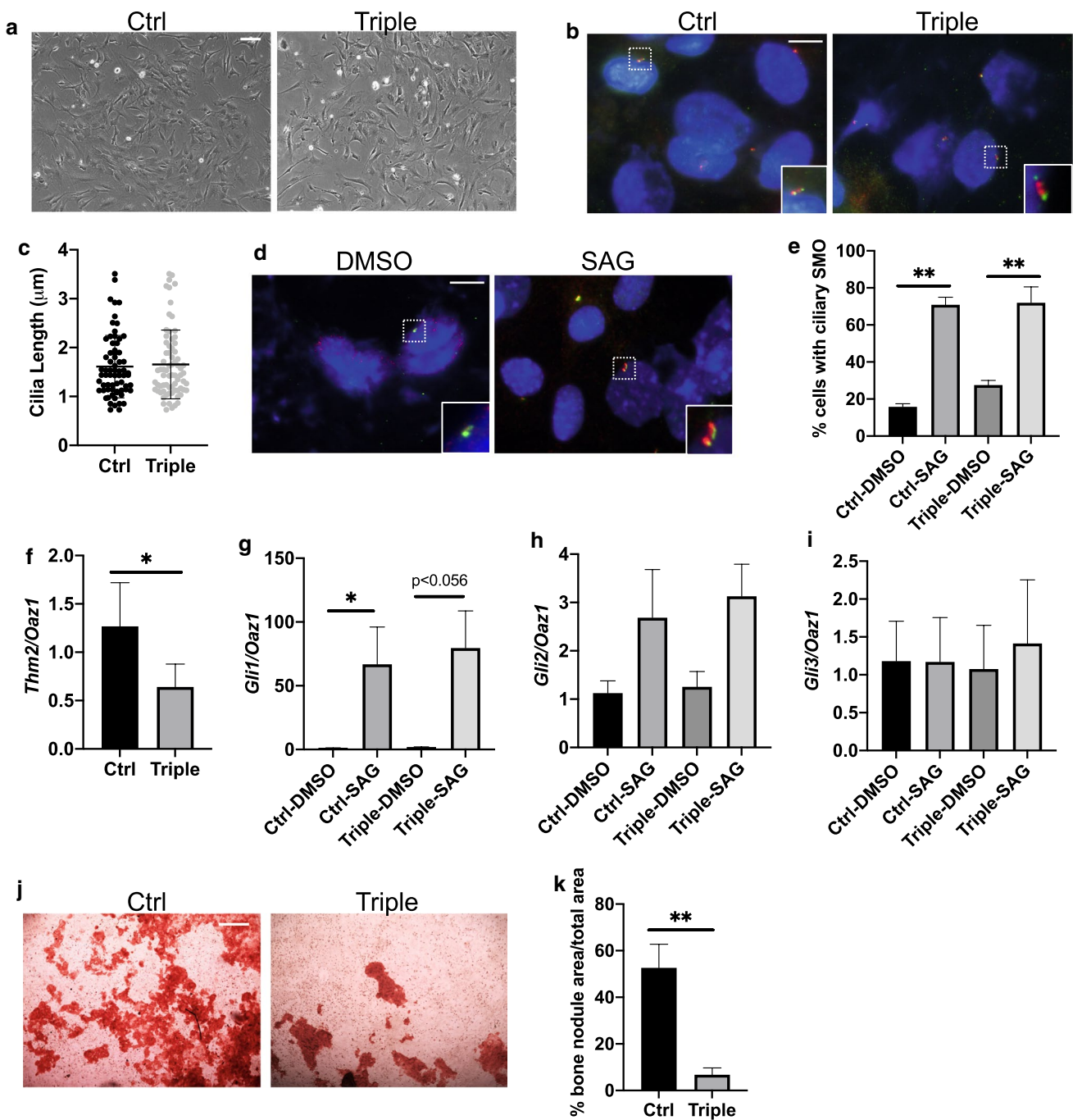
Fig. 10 *Thm2^−/−; Thm1^aln/+* osteoblasts show defective differentiation. **a** Phase contrast images of calvarial-derived primary osteoblasts. Scale bar—100 μm. **b** Immunostaining for acetylated α-tubulin (red) and IFT81 (green). Scale bar—10 μm. **c** Quantification of ciliary lengths. Error bars represent mean ± SD from $n=3$ ctrl and $n=3$ triple allele mutant mice. **d** Ciliary localization of SMO (red) and ARL13B (green) in response to vehicle (DMSO) or SAG. Scale bar—10 μm. **e** Quantification of proportion of cells with ciliary SMO. Bar graphs represent mean ± SEM from cell cultures of $n=3$ ctrl and $n=3$ triple allele mutant mice. **f** qPCR for *Thm2*; **g** *Gli1*; **h** *Gli2*; **i** *Gli3* relative to *Oaz1*. Bar graphs represent mean ± SEM from cell cultures of $n=4$ ctrl and $n=4$ triple allele mutant mice. **j** Alizarin red staining following bone nodule formation assay. Scale bar—500 μm. **k** Quantification of bone nodule formation of cell cultures from $n=4$ ctrl and $n=4$ triple allele mutant mice. Statistical significance was determined using one-way ANOVA and Tukey's test for **e**, **g–i**, and using two-tailed, unpaired t test for **f** and **k**. $*p < 0.05$; $**p < 0.01$

Compliance with ethical standards

References

1. Xiao Z, Zhang S, Mahlios J, Zhou G, Magenheimer BS, Guo D, Dallas SL, Maser R, Calvet JP, Bonewald L, Quarles LD (2006) Cilia-like structures and polycystin-1 in osteoblasts/osteocytes and associated abnormalities in skeletogenesis and Runx2 expression. J Biol Chem 281(41):30884–30895. https://doi.org/10.1074/jbc.M604772200

2. Song B, Haycraft CJ, Seo HS, Yoder BK, Serra R (2007) Development of the post-natal growth plate requires intraflagellar transport proteins. Dev Biol 305(1):202–216. https://doi.org/10.1016/j.ydbio.2007.02.003

3. Quinlan RJ, Tobin JL, Beales PL (2008) Modeling ciliopathies: primary cilia in development and disease. Curr Top Dev Biol 84:249–310. https://doi.org/10.1016/s0070-2153(08)00605-4

4. Halbritter J, Bizet AA, Schmidts M, Porath JD, Braun DA, Gee HY, McInerney-Leo AM, Krug P, Filhol E, Davis EE, Airik R, Czarnecki PG, Lehman AM, Trnka P, Nitschke P, Bole-Feysot C, Schueler M, Knebelmann B, Burtey S, Szabo AJ, Tory K, Leo PJ, Gardiner B, McKenzie FA, Zankl A, Brown MA, Hartley JL, Maher ER, Li C, Leroux MR, Scambler PJ, Zhan SH, Jones SJ, Kayserili H, Tuysuz B, Moorani KN, Constantinescu A, Krantz ID, Kaplan BS, Shah JV, Consortium UK, Hurd TW, Doherty D, Katsanis N, Duncan EL, Otto EA, Beales PL, Mitchison HM, Saunier S, Hildebrandt F (2013) Defects in the IFT-B component IFT172 cause Jeune and Mainzer-Saldino syndromes in humans. Am J Hum Genet 93(5):915–925. https://doi.org/10.1016/j.ajhg.2013.09.012

5. Veland IR, Awan A, Pedersen LB, Yoder BK, Christensen ST (2009) Primary cilia and signaling pathways in mammalian development, health and disease. Nephron Physiol 111(3):p39-53. https://doi.org/10.1159/000208212

6. Valente EM, Rosti RO, Gibbs E, Gleeson JG (2014) Primary cilia in neurodevelopmental disorders. Nat Rev Neurol 10(1):27–36. https://doi.org/10.1038/nrneurol.2013.247

7. Mukhopadhyay S, Wen X, Chih B, Nelson CD, Lane WS, Scales SJ, Jackson PK (2010) TULP3 bridges the IFT-A complex and membrane phosphoinositides to promote trafficking of G protein-coupled receptors into primary cilia. Genes Dev 24(19):2180–2193. https://doi.org/10.1101/gad.1966210

8. Liem KF Jr, Ashe A, He M, Satir P, Moran J, Beier D, Wicking C, Anderson KV (2012) The IFT-A complex regulates Shh signaling through cilia structure and membrane protein trafficking. J Cell Biol 197(6):789–800. https://doi.org/10.1083/jcb.201110049

9. Hirano T, Katoh Y, Nakayama K (2017) Intraflagellar transport-A complex mediates ciliary entry and retrograde trafficking of ciliary G protein-coupled receptors. Mol Biol Cell 28(3):429–439. https://doi.org/10.1091/mbc.E16-11-0813

10. Picariello T, Brown JM, Hou Y, Swank G, Cochran DA, King OD, Lechtreck K, Pazour GJ, Witman GB (2019) A global analysis of IFT-A function reveals specialization for transport of membrane-associated proteins into cilia. J Cell Sci. https://doi.org/10.1242/jcs.220749

11. Goetz SC, Anderson KV (2010) The primary cilium: a signalling centre during vertebrate development. Nat Rev Genet 11(5):331–344. https://doi.org/10.1038/nrg2774

12. Corbit KC, Aanstad P, Singla V, Norman AR, Stainier DY, Reiter JF (2005) Vertebrate smoothened functions at the primary cilium. Nature 437(7061):1018–1021. https://doi.org/10.1038/nature04117

13. Haycraft CJ, Banizs B, Aydin-Son Y, Zhang Q, Michaud EJ, Yoder BK (2005) Gli2 and Gli3 localize to cilia and require the intraflagellar transport protein polaris for processing and function. PLoS Genet 1(4):e53. https://doi.org/10.1371/journal.pgen.0010053

14. Huangfu D, Liu A, Rakeman AS, Murcia NS, Niswander L, Anderson KV (2003) Hedgehog signalling in the mouse requires intraflagellar transport proteins. Nature 426(6962):83–87. https://doi.org/10.1038/nature02061

15. Arsov T, Silva DG, O'Bryan MK, Sainsbury A, Lee NJ, Kennedy C, Manji SS, Nelms K, Liu C, Vinuesa CG, de Kretser DM, Goodnow CC, Petrovsky N (2006) Fat aussie—a new Alstrom syndrome mouse showing a critical role for ALMS1 in obesity, diabetes, and spermatogenesis. Mol Endocrinol 20(7):1610–1622. https://doi.org/10.1210/me.2005-0494

16. Huangfu D, Anderson KV (2005) Cilia and Hedgehog responsiveness in the mouse. Proc Natl Acad Sci USA 102(32):11325–11330. https://doi.org/10.1073/pnas.0505328102

17. Tran PV, Haycraft CJ, Besschetnova TY, Turbe-Doan A, Stottmann RW, Herron BJ, Chesebro AL, Qiu H, Scherz PJ, Shah JV, Yoder BK, Beier DR (2008) THM1 negatively modulates mouse sonic

hedgehog signal transduction and affects retrograde intraflagellar transport in cilia. Nat Genet 40(4):403–410. https://doi.org/10.1038/ng.105

18. Davis EE, Zhang Q, Liu Q, Diplas BH, Davey LM, Hartley J, Stoetzel C, Szymanska K, Ramaswami G, Logan CV, Muzny DM, Young AC, Wheeler DA, Cruz P, Morgan M, Lewis LR, Cherukuri P, Maskeri B, Hansen NF, Mullikin JC, Blakesley RW, Bouffard GG, Gyapay G, Rieger S, Tonshoff B, Kern I, Soliman NA, Neuhaus TJ, Swoboda KJ, Kayserili H, Gallagher TE, Lewis RA, Bergmann C, Otto EA, Saunier S, Scambler PJ, Beales PL, Gleeson JG, Maher ER, Attie-Bitach T, Dollfus H, Johnson CA, Green ED, Gibbs RA, Hildebrandt F, Pierce EA, Katsanis N (2011) TTC21B contributes both causal and modifying alleles across the ciliopathy spectrum. Nat Genet 43(3):189–196. https://doi.org/10.1038/ng.756

19. Chang CF, Chang YT, Millington G, Brugmann SA (2016) Craniofacial ciliopathies reveal specific requirements for GLI proteins during development of the facial midline. PLoS Genet 12(11):e1006351. https://doi.org/10.1371/journal.pgen.1006351

20. Driver AM, Shumrick C, Stottmann RW (2017) Ttc21b is required in bergmann glia for proper granule cell radial migration. J Dev Biol. https://doi.org/10.3390/jdb5040018

21. Arts HH, Bongers EM, Mans DA, van Beersum SE, Oud MM, Bolat E, Spruijt L, Cornelissen EA, Schuurs-Hoeijmakers JH, de Leeuw N, Cormier-Daire V, Brunner HG, Knoers NV, Roepman R (2011) C14ORF179 encoding IFT43 is mutated in Sensenbrenner syndrome. J Med Genet 48(6):390–395. https://doi.org/10.1136/jmg.2011.088864

22. Duran I, Taylor SP, Zhang W, Martin J, Qureshi F, Jacques SM, Wallerstein R, Lachman RS, Nickerson DA, Bamshad M, Cohn DH, Krakow D (2017) Mutations in IFT-A satellite core component genes IFT43 and IFT121 produce short rib polydactyly syndrome with distinctive campomelia. Cilia 6:7. https://doi.org/10.1186/s13630-017-0051-y

23. Walczak-Sztulpa J, Eggenschwiler J, Osborn D, Brown DA, Emma F, Klingenberg C, Hennekam RC, Torre G, Garshasbi M, Tzschach A, Szczepanska M, Krawczynski M, Zachwieja J, Zwolinska D, Beales PL, Ropers HH, Latos-Bielenska A, Kuss AW (2010) Cranioectodermal dysplasia, sensenbrenner syndrome, is a ciliopathy caused by mutations in the IFT122 gene. Am J Hum Genet 86(6):949–956. https://doi.org/10.1016/j.ajhg.2010.04.012

24. Alazami AM, Seidahmed MZ, Alzahrani F, Mohammed AO, Alkuraya FS (2014) Novel IFT122 mutation associated with impaired ciliogenesis and cranioectodermal dysplasia. Mol Genet Genomic Med 2(2):103–106. https://doi.org/10.1002/mgg3.44

25. Bredrup C, Saunier S, Oud MM, Fiskerstrand T, Hoischen A, Brackman D, Leh SM, Midtbo M, Filhol E, Bole-Feysot C, Nitschke P, Gilissen C, Haugen OH, Sanders JS, Stolte-Dijkstra I, Mans DA, Steenbergen EJ, Hamel BC, Matignon M, Pfundt R, Jeanpierre C, Boman H, Rodahl E, Veltman JA, Knappskog PM, Knoers NV, Roepman R, Arts HH (2011) Ciliopathies with skeletal anomalies and renal insufficiency due to mutations in the IFT-A gene WDR19. Am J Hum Genet 89(5):634–643. https://doi.org/10.1016/j.ajhg.2011.10.001

26. Perrault I, Saunier S, Hanein S, Filhol E, Bizet AA, Collins F, Salih MA, Gerber S, Delphin N, Bigot K, Orssaud C, Silva E, Baudouin V, Oud MM, Shannon N, Le Merrer M, Roche O, Pietrement C, Goumid J, Baumann C, Bole-Feysot C, Nitschke P, Zahrate M, Beales P, Arts HH, Munnich A, Kaplan J, Antignac C, Cormier-Daire V, Rozet JM (2012) Mainzer-Saldino syndrome is a ciliopathy caused by IFT140 mutations. Am J Hum Genet 90(5):864–870. https://doi.org/10.1016/j.ajhg.2012.03.006

27. Belgacem YH, Borodinsky LN (2011) Sonic hedgehog signaling is decoded by calcium spike activity in the developing spinal cord. Proc Natl Acad Sci USA 108(11):4482–4487. https://doi.org/10.1073/pnas.1018217108

28. Beales PL, Bland E, Tobin JL, Bacchelli C, Tuysuz B, Hill J, Rix S, Pearson CG, Kai M, Hartley J, Johnson C, Irving M, Elcioglu N, Winey M, Tada M, Scambler PJ (2007) IFT80, which encodes a conserved intraflagellar transport protein, is mutated in Jeune asphyxiating thoracic dystrophy. Nat Genet 39(6):727–729. https://doi.org/10.1038/ng2038

29. Girisha KM, Shukla A, Trujillano D, Bhavani GS, Hebbar M, Kadavigere R, Rolfs A (2016) A homozygous nonsense variant in IFT52 is associated with a human skeletal ciliopathy. Clin Genet 90(6):536–539. https://doi.org/10.1111/cge.12762

30. Zhang W, Taylor SP, Nevarez L, Lachman RS, Nickerson DA, Bamshad M, University of Washington Center for Mendelian Genomics C, Krakow D, Cohn DH (2016) IFT52 mutations destabilize anterograde complex assembly, disrupt ciliogenesis and result in short rib polydactyly syndrome. Hum Mol Genet 25(18):4012–4020. https://doi.org/10.1093/hmg/ddw241

31. Shaheen R, Alsahli S, Ewida N, Alzahrani F, Shamseldin HE, Patel N, Al Qahtani A, Alhebbi H, Alhashem A, Al-Sheddi T, Alomar R, Alobeid E, Abouelhoda M, Monies D, Al-Hussaini A, Alzouman MA, Shagrani M, Faqeih E, Alkuraya FS (2020) Biallelic mutations in tetratricopeptide repeat domain 26 (Intraflagellar Transport 56) cause severe biliary ciliopathy in humans. Hepatology 71(6):2067–2079. https://doi.org/10.1002/hep.30982

32. Herron BJ, Lu W, Rao C, Liu S, Peters H, Bronson RT, Justice MJ, McDonald JD, Beier DR (2002) Efficient generation and mapping of recessive developmental mutations using ENU mutagenesis. Nat Genet 30(2):185–189. https://doi.org/10.1038/ng812

33. Miller KA, Ah-Cann CJ, Welfare MF, Tan TY, Pope K, Caruana G, Freckmann ML, Savarirayan R, Bertram JF, Dobbie MS, Bateman JF, Farlie PG (2013) Cauli: a mouse strain with an Ift140 mutation that results in a skeletal ciliopathy modelling Jeune syndrome. PLoS Genet 9(8):e1003746. https://doi.org/10.1371/journal.pgen.1003746

34. Ashe A, Butterfield NC, Town L, Courtney AD, Cooper AN, Ferguson C, Barry R, Olsson F, Liem KF Jr, Parton RG, Wainwright BJ, Anderson KV, Whitelaw E, Wicking C (2012) Mutations in mouse Ift144 model the craniofacial, limb and rib defects in skeletal ciliopathies. Hum Mol Genet 21(8):1808–1823. https://doi.org/10.1093/hmg/ddr613

35. Rix S, Calmont A, Scambler PJ, Beales PL (2011) An Ift80 mouse model of short rib polydactyly syndromes shows defects in hedgehog signalling without loss or malformation of cilia. Hum Mol Genet 20(7):1306–1314. https://doi.org/10.1093/hmg/ddr013

36. Haycraft CJ, Zhang Q, Song B, Jackson WS, Detloff PJ, Serra R, Yoder BK (2007) Intraflagellar transport is essential for endochondral bone formation. Development 134(2):307–316. https://doi.org/10.1242/dev.02732

37. Drera B, Ferrari D, Cavalli P, Poggiani C (2014) A case of neonatal Jeune syndrome expanding the phenotype. Clin Case Rep 2(4):156–158. https://doi.org/10.1002/ccr3.85

38. Liu W, He X, Yang S, Zouari R, Wang J, Wu H, Kherraf ZE, Liu C, Coutton C, Zhao R, Tang D, Tang S, Lv M, Fang Y, Li W, Li H, Zhao J, Wang X, Zhao S, Zhang J, Arnoult C, Jin L, Zhang Z, Ray PF, Cao Y, Zhang F (2019) Bi-allelic Mutations in TTC21A induce asthenoteratospermia in humans and mice. Am J Hum Genet 104(4):738–748. https://doi.org/10.1016/j.ajhg.2019.02.020

39. Shimada A, Komatsu K, Nakashima K, Poschl E, Nifuji A (2012) Improved methods for detection of beta-galactosidase (lacZ) activity in hard tissue. Histochem Cell Biol 137(6):841–847. https://doi.org/10.1007/s00418-012-0936-1

40. Belluoccio D, Etich J, Rosenbaum S, Frie C, Grskovic I, Stermann J, Ehlen H, Vogel S, Zaucke F, von der Mark K, Bateman JF, Brachvogel B (2010) Sorting of growth plate chondrocytes allows the isolation and characterization of cells of a defined differentiation status. J Bone Miner Res 25(6):1267–1281. https://doi.org/10.1002/jbmr.30

41. Dallas SL, Miyazono K, Skerry TM, Mundy GR, Bonewald LF (1995) Dual role for the latent transforming growth factor-beta binding protein in storage of latent TGF-beta in the extracellular matrix and as a structural matrix protein. J Cell Biol 131(2):539–549. https://doi.org/10.1083/jcb.131.2.539

42. Qin J, Lin Y, Norman RX, Ko HW, Eggenschwiler JT (2011) Intraflagellar transport protein 122 antagonizes Sonic Hedgehog signaling and controls ciliary localization of pathway components. Proc Natl Acad Sci USA 108(4):1456–1461. https://doi.org/10.1073/pnas.1011410108

43. Park HL, Bai C, Platt KA, Matise MP, Beeghly A, Hui CC, Nakashima M, Joyner AL (2000) Mouse Gli1 mutants are viable but have defects in SHH signaling in combination with a Gli2 mutation. Development 127(8):1593–1605

44. Abbasi AA, Goode DK, Amir S, Grzeschik KH (2009) Evolution and functional diversification of the GLI family of transcription factors in vertebrates. Evol Bioinform Online 5:5–13. https://doi.org/10.4137/ebo.s2322

45. Kronenberg HM (2003) Developmental regulation of the growth plate. Nature 423(6937):332–336. https://doi.org/10.1038/nature01657

46. Yuan X, Yang S (2016) Primary cilia and intraflagellar transport proteins in bone and cartilage. J Dent Res 95(12):1341–1349. https://doi.org/10.1177/0022034516652383

47. Mo R, Freer AM, Zinyk DL, Crackower MA, Michaud J, Heng HH, Chik KW, Shi XM, Tsui LC, Cheng SH, Joyner AL, Hui C (1997) Specific and redundant functions of Gli2 and Gli3 zinc finger genes in skeletal patterning and development. Development 124(1):113–123

48. Tao D, Xue H, Zhang C, Li G, Sun Y (2019) The role of IFT140 in osteogenesis of adult mice long bone. J Histochem Cytochem 67(8):601–611. https://doi.org/10.1369/0022155419847188

49. Rauch A, Thiel CT, Schindler D, Wick U, Crow YJ, Ekici AB, van Essen AJ, Goecke TO, Al-Gazali L, Chrzanowska KH, Zweier C, Brunner HG, Becker K, Curry CJ, Dallapiccola B, Devriendt K, Dorfler A, Kinning E, Megarbane A, Meinecke P, Semple RK, Spranger S, Toutain A, Trembath RC, Voss E, Wilson L, Hennekam R, de Zegher F, Dorr HG, Reis A (2008) Mutations in the pericentrin (PCNT) gene cause primordial dwarfism. Science 319(5864):816–819. https://doi.org/10.1126/science.1151174

50. Kalay E, Yigit G, Aslan Y, Brown KE, Pohl E, Bicknell LS, Kayserili H, Li Y, Tuysuz B, Nurnberg G, Kiess W, Koegl M, Baessmann I, Buruk K, Toraman B, Kayipmaz S, Kul S, Ikbal M, Turner DJ, Taylor MS, Aerts J, Scott C, Milstein K, Dollfus H, Wieczorek D, Brunner HG, Hurles M, Jackson AP, Rauch A, Nurnberg P, Karaguzel A, Wollnik B (2011) CEP152 is a genome maintenance protein disrupted in Seckel syndrome. Nat Genet 43(1):23–26. https://doi.org/10.1038/ng.725

51. Al-Dosari MS, Shaheen R, Colak D, Alkuraya FS (2010) Novel CENPJ mutation causes Seckel syndrome. J Med Genet 47(6):411–414. https://doi.org/10.1136/jmg.2009.076646

52. Fu W, Wang L, Kim S, Li J, Dynlacht BD (2016) Role for the IFT-A complex in selective transport to the primary cilium. Cell Rep 17(6):1505–1517. https://doi.org/10.1016/j.celrep.2016.10.018

53. Wang B, Fallon JF, Beachy PA (2000) Hedgehog-regulated processing of Gli3 produces an anterior/posterior repressor gradient in the developing vertebrate limb. Cell 100(4):423–434

54. Tran PV, Talbott GC, Turbe-Doan A, Jacobs DT, Schonfeld MP, Silva LM, Chatterjee A, Prysak M, Allard BA, Beier DR (2014) Downregulating hedgehog signaling reduces renal cystogenic potential of mouse models. J Am Soc Nephrol 25(10):2201–2212. https://doi.org/10.1681/ASN.2013070735

55. St-Jacques B, Hammerschmidt M, McMahon AP (1999) Indian hedgehog signaling regulates proliferation and differentiation of chondrocytes and is essential for bone formation. Genes Dev 13(16):2072–2086. https://doi.org/10.1101/gad.13.16.2072

56. Hsu SH, Zhang X, Cheng S, Wunder JS, Hui CC, Alman BA (2012) Suppressor of fused (Sufu) mediates the effect of parathyroid hormone-like hormone (Pthlh) on chondrocyte differentiation in the growth plate. J Biol Chem 287(43):36222–36228. https://doi.org/10.1074/jbc.M112.382275

57. Yang J, Andre P, Ye L, Yang YZ (2015) The Hedgehog signalling pathway in bone formation. Int J Oral Sci 7(2):73–79. https://doi.org/10.1038/ijos.2015.14

58. Schock EN, Struve JN, Chang CF, Williams TJ, Snedeker J, Attia AC, Stottmann RW, Brugmann SA (2017) A tissue-specific role for intraflagellar transport genes during craniofacial development. PLoS ONE 12(3):e0174206. https://doi.org/10.1371/journal.pone.0174206

59. Wang W, Allard BA, Pottorf TS, Wang HH, Vivian JL, Tran PV (2020) Genetic interaction of mammalian IFT-A paralogs regulates cilia disassembly, ciliary entry of membrane protein, Hedgehog signaling, and embryogenesis. FASEB J. https://doi.org/10.1096/fj.201902611R

60. Sanford LP, Ormsby I, Gittenberger-de Groot AC, Sariola H, Friedman R, Boivin GP, Cardell EL, Doetschman T (1997) TGFbeta2 knockout mice have multiple developmental defects that are non-overlapping with other TGFbeta knockout phenotypes. Development 124(13):2659–2670

61. Ji Y, Ke Y, Gao S (2017) Intermittent activation of notch signaling promotes bone formation. Am J Transl Res 9(6):2933–2944

62. Tao J, Chen S, Lee B (2010) Alteration of notch signaling in skeletal development and disease. Ann N Y Acad Sci 1192:257–268. https://doi.org/10.1111/j.1749-6632.2009.05307.x

63. Zhong Z, Ethen NJ, Williams BO (2014) WNT signaling in bone development and homeostasis. Wiley Interdiscip Rev Dev Biol 3(6):489–500. https://doi.org/10.1002/wdev.159

64. Keady BT, Samtani R, Tobita K, Tsuchya M, San Agustin JT, Follit JA, Jonassen JA, Subramanian R, Lo CW, Pazour GJ (2012) IFT25 links the signal-dependent movement of Hedgehog components to intraflagellar transport. Dev Cell 22(5):940–951. https://doi.org/10.1016/j.devcel.2012.04.009

65. Yoon J, Comerci CJ, Weiss LE, Milenkovic L, Stearns T, Moerner WE (2019) Revealing nanoscale morphology of the primary cilium using super-resolution fluorescence microscopy. Biophys J 116(2):319–329. https://doi.org/10.1016/j.bpj.2018.11.3136

66. Xin D, Christopher KJ, Zeng L, Kong Y, Weatherbee SD (2017) IFT56 regulates vertebrate developmental patterning by maintaining IFTB complex integrity and ciliary microtubule architecture. Development 144(8):1544–1553. https://doi.org/10.1242/dev.143255

67. Dmitriev AA, Rudenko EE, Kudryavtseva AV, Krasnov GS, Gordiyuk VV, Melnikova NV, Stakhovsky EO, Kononenko OA, Pavlova LS, Kondratieva TT, Alekseev BY, Braga EA, Senchenko VN, Kashuba VI (2014) Epigenetic alterations of chromosome 3 revealed by NotI-microarrays in clear cell renal cell carcinoma. Biomed Res Int 2014:735292. https://doi.org/10.1155/2014/735292

68. Wang W, Ren S, Wang Z, Zhang C, Huang J (2020) Increased expression of TTC21A in lung adenocarcinoma infers favorable prognosis and high immune infiltrating level. Int Immunopharmacol 78:106077. https://doi.org/10.1016/j.intimp.2019.106077

69. Li S, Weinstein G, Zare H, Teumer A, Volker U, Friedrich N, Knol MJ, Satizabal CL, Petyuk VA, Adams HHH, Launer LJ, Bennett DA, De Jager PL, Grabe HJ, Ikram MA, Gudnason V, Yang Q, Seshadri S (2020) The genetics of circulating BDNF: towards understanding the role of BDNF in brain structure and function in middle and old ages. Brain Commun 2(2):fcaa176. https://doi.org/10.1093/braincomms/fcaa176

Publisher's Note Springer Nature remains neutral with regard to jurisdictional claims in published maps and institutional affiliations.